Monthly Notices
of the
ROYAL ASTRONOMICAL SOCIETY

MNRAS **474,** 647–661 (2018) doi:10.1093/mnras/stx2676

A multi-wavelength analysis of the diffuse H II region G25.8700+0.1350

S. Cichowolski,[1⋆] N. U. Duronea,[2⋆†] L. A. Suad,[2†] E. M. Reynoso[1†] and R. Dorda[3]

[1]*Instituto de Astronomía y Física del Espacio (UBA, CONICET), CC 67, Suc. 28, 1428 Buenos Aires, Argentina*
[2]*Instituto Argentino de Radioastronomía (CCT-La Plata, CONICET; CICPBA), C.C. No. 5, 1894,Villa Elisa, Argentina*
[3]*Departamento de Física, Ingeniería de Sistemas y Teoría de la Señal, Universidad de Alicante, Carretera de San Vicente del Raspeig, E-03690 Alicante, Spain*

Accepted 2017 October 9. Received 2017 October 9; in original form 2017 July 12

ABSTRACT

We present a multi-wavelength investigation of the H II region G25.8700+0.1350, located in the inner part of the Galaxy. In radio continuum emission, the region is seen as a bright arc-shaped structure. An analysis of the H I line suggests that G25.8700+0.1350 lies at a distance of 6.5 kpc. The ionized gas is bordered by a photodissociation region, which is encircled by a molecular structure where four molecular clumps are detected. At infrared wavelengths, the region is also very conspicuous. Given the high level of visual absorption in the region, the exciting stars should be searched for in the infrared band. In this context, we found in the literature one Wolf–Rayet and one red supergiant, which, together with 37 2MASS sources that are candidate O-type stars, could be related to the origin of G25.8700+0.1350. Finally, as expanding H II regions are hypothesized to trigger star formation, we used different infrared point source catalogues to search for young stellar object candidates (cYSOs). A total of 45 cYSOs were identified projected on to the molecular clouds.

Key words: stars: formation – stars: massive – ISM: bubbles – H II regions – infrared: ISM.

1 INTRODUCTION

Massive stars are known to play an important role in disrupting, modifying and dispersing the ambient molecular gas through their ultraviolet (UV) radiation, strong winds, outflows and eventually, with supernova explosions. The strong UV radiation of massive stars ionizes the molecular gas, creating H II regions, which are expected to expand in the interstellar medium (ISM) because of the high difference in pressure between the ionized and the ambient neutral gas. This can produce large distortions in their surroundings and even compression of nearby molecular clouds, stimulating the formation of a new generation of stars (Elmegreen & Lada 1977; Lefloch & Lazareff 1994; Zinnecker & Yorke 2007).

The feedback from massive stars and the evolution of their associated H II regions determine the physical conditions of their environs and the star formation rate in the region. Hence, it is important to study the ISM adjacent to Galactic H II regions since they can provide substantial information about the physical conditions where massive stars are born and they can be used to set empirical constraints on existing theoretical models and to improve our knowledge of the physical processes leading to stellar formation and evolution.

In this paper, we present the very first multi-wavelength analysis of the diffuse H II region catalogued by Helfand et al. (2006) as G25.8700+0.1350. This region consists of a large bright partial arc in the inner Galaxy near the tangent point as inferred from observations in several radio recombination lines (RRLs). This H II region is especially interesting because it is close to two young high-mass clusters, RSGC1 (Figer et al. 2006; Davies et al. 2008) and RSGC2 (Davies et al. 2007), which are dominated by red supergiants (RSGs), a type of evolved high-mass stars. These clusters are separated from the centre of G25.8700+0.1350 by 39.8 and 22.6 arcmin, respectively. Moreover, the largest concentration of RSGs known in our Galaxy (Negueruela et al. 2012; Dorda et al. 2016) can be found around these clusters. According to the high density of RSGs, this region is probably one of the most intense star-forming places in the Galaxy.

2 DATA SETS

To carry out this study, we made use of public archival data from near-infrared (IR) to radio wavelengths. In the following, we describe the data sets employed:

(i) Radio continuum data at 1420 MHz were extracted from the Multi-Array Galactic Plane Imaging Survey (MAGPIS; Helfand

⋆ E-mail: scicho@iafe.uba.ar (SC); duronea@iar.unlp.edu.ar (NUD)
† Member of the Carrera del Investigador Científico of CONICET, Argentina.

et al. 2006). This survey was constructed by combining Very Large Array (VLA) observations in the B, C and D arrays. VLA data have a limited u, v coverage and are insensitive to structures much larger than 1 arcmin. Hence, the MAGPIS images include short spatial frequencies obtained from observations with the 100-m Effelsberg radio telescope so as to sample all diffuse, extended structures. The angular resolution is 6.2 × 5.4 arcsec and the sensitivity, 0.2 mJy beam^{-1}.

(ii) IR data were obtained from the Herschel Infrared Galactic Plane Survey (Hi-Gal). Hi-Gal (Molinari et al. 2010) used the Photodetector Array Camera and Spectrometer (PACS; Poglitsch et al. 2010) and the Spectral and Photometric Imaging Receiver (SPIRE; Griffin et al. 2010) cameras. The instruments detect emissions at 70 and 160 μm (PACS) and 250 μm (SPIRE) and have an angular resolutions of 5.5, 12 and 17 arcsec, respectively. We obtained the UNIMAP level 2.5 images using the Herschel Science Archive.[1] We complemented IR emission data using data from the *Spitzer Space Telescope*. We used the emission at 8 μm from the Infrared Array Camera (IRAC; Werner et al. 2004), and 24 μm from the Multiband Imaging Photometer (MIPS; Rieke et al. 2004). The spatial resolutions are 2 and 6 arcsec for 8 and 24 μm, respectively.

(iii) We used H I 21 cm data from the VLA Galactic Plane Survey (VGPS; Stil et al. 2006). As for MAGPIS, the interferometric data must be completed with short spacings to sample extended structures. In this survey, single dish data were supplied by the Green Bank Telescope. The H I line data of VGPS have an angular resolution of 1 × 1 arcmin and a spectral resolution of 1.56 km s^{-1}, although channels are sampled each 0.824 km s^{-1} for consistency with the Canadian Galactic Plane Survey.

(iv) To survey the molecular emission, we used ^{13}CO(1-0) line data obtained from the Boston University-FCRAO Galactic Ring Survey[2] (Jackson et al. 2006) carried out with the SEQUOIA multi-pixel array receiver on the FCRAO 14-m telescope. This survey covers the Galactic plane in the range $18.0 < l < 55.7^\circ$ and $-1.0 < b < 1.0^\circ$, and has a sensitivity of <0.4 K. The angular resolution and sampling are 46 and 22 arcsec, respectively. The velocity resolution is 0.2 km s^{-1}, covering a range from −5 to +135 km s^{-1}. We also used CO(3-2) line data obtained from the CO High-Resolution Survey[3] (Dempsey, Thomas & Currie 2013). The data were taken using the Heterodyne Array Receiver Programme on the James Clerk Maxwell Telescope. The angular resolution and sampling are 14 and 6 arcsec, respectively. The velocity resolution is 1 km s^{-1}, spanning from −30 to +155 km s^{-1}.

(v) We used 1.1 mm continuum data from the Bolocam Galactic Plane Survey.[4] This survey is contiguous over the range $-10.5 \leq l \leq 90.5^\circ$, $|b| \leq 0.5^\circ$, and is extended to $|b| \leq 1.5^\circ$ for $75.5 \leq l \leq 87.5^\circ$. Additional cross-cuts were performed at $l = 3.0^\circ$, 15.0°, 30.0° and 31.0°, and four supplementary regions of the outer Galaxy, covering 170 deg^2 in total (Aguirre et al. 2011). Bolocam is a 144-element bolometer array camera mounted at the Cassegrain focus of the 10.4-m mirror of the Caltech Submillimeter Observatory on the summit of Mauna Kea. The array field of view of the instrument is 7.5 arcmin, and its effective resolution is 33 arcsec (Glenn et al. 2003).

[1] http://www.cosmos.esa.int/web/herschel/science-archive
[2] http://www.bu.edu/galacticring/new_index.htm
[3] http://dx.doi.org/10.11570/13.0002
[4] http://irsa.ipac.caltech.edu/Missions/bolocam.html

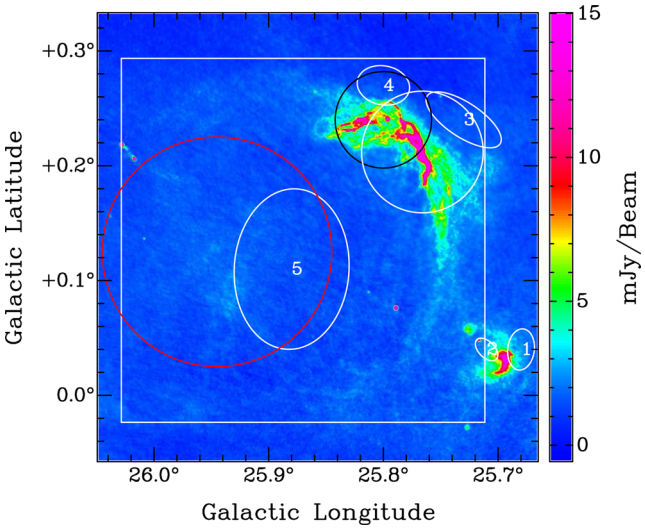

Figure 1. Radio continuum image of the region at 1420 MHz obtained from MAGPIS. The box indicates the location of G25.8700+0.1350. The red, black and white circles indicate where RRLs were detected by Lockman et al. (1996), Sewilo et al. (2004) and Quireza et al. (2006a), respectively. The size of the circles corresponds to the beam size of each observation. The ellipses, numbered as in Table 1, enclose the ionized regions having associated CO, as indicated by Anderson & Bania (2009).

3 G25.8700+0.1350 AND ITS LOCAL ISM

Fig. 1 shows the emission distribution of the region under study at 1420 MHz. G25.8700+0.1350 is a large bright source, whose location and size, as given by Helfand et al. (2006), are indicated by the box. Several RRLs have been detected in the region (see Fig. 1). Lockman, Pisano & Howard (1996) detected the 6 cm (H109α and H111α) RRL at (l, b) = (25.945°, +0.125°) at a velocity of 104.0 ± 1.1 km s^{-1}. The 110 Hα line was detected at (l, b) = (25.8°, +0.24°) at a velocity of 112.1 ± 0.1 km s^{-1} by Sewilo et al. (2004). Finally, Quireza et al. (2006a) detected towards (l, b) = (25.766°, +0.212°), the 91α and 92α lines of H, He and C at 111.44 ± 0.17 km s^{-1}, 111.35 ± 1.89 km s^{-1} and 124.52 ± 0.96 km s^{-1}, respectively.

Since G25.8700+0.1350 is in the first Galactic quadrant, two distances, near (N) and far (F), are possible for each radial velocity up to the tangent point. Resolving the kinematic distance ambiguity (KDA) is not easy, especially when the radial velocity of the source is very close to the velocity of the tangent point (T). The most straightforward method for solving the KDA for H II regions consists of constructing a 21 cm H I absorption spectrum towards the radio continuum emission and comparing the absorption features with corresponding H I emission peaks. The last emission feature detected indicates the velocity of the tangent point. The detection of H I absorption up to the tangent point implies that the source lies at the far distance inferred from the RRL velocity. Otherwise, it is safe to assume that the H II region is located at a near distance.

In the direction of G25.8700+0.1350, the velocity of the tangent point is about +125 km s^{-1}, and the corresponding kinematic distance is around 7.7 kpc. Several attempts to solve for the KDA in G25.8700+0.1350 are described in the literature. Applying the canonical method described above, Quireza et al. (2006b) inferred that the region is at 7.3 kpc, which corresponds to the near distance. On the other hand, Sewilo et al. (2004) used H_2CO line observations to disentangle the KDA problem for several H II regions. For G25.8700+0.1350, they cannot unambiguously distinguish

Table 1. Parameters of H II regions associated with CO clouds.

	ID	l (°)	b (°)	V_{LSR} (km s^{-1})	EA	Q-EA	SA	Q-SA	D (kpc)
1	U25.72+0.05a	25.72	0.05	53.3	–	–	N	B	3.6
2	U25.72+0.05b	25.72	0.05	102.0	–	–	F	A	9.2
3	C25.77+0.21	25.77	0.21	110.8	T	–	N	A	6.7
4	U25.80+0.24	25.80	0.24	112.1	T	–	N	A	6.8[a]
5	D25.94+0.10	25.94	0.10	104.0	T	–	F	B	9.1

Note: [a]The distance information given for this source is confusing since its radial velocity was not properly taken from the work of Anderson et al. (2009). We adopt the near distance associated with $V_{LSR} = 112.1$ km s^{-1} instead of the one given by Anderson & Bania (2009), i.e. 7.7 kpc.

between the near and far positions. Finally, Anderson & Bania (2009) resolved the KDA using H I and ^{13}CO surveys for 266 H II regions located in the inner Galaxy with RRL emission detected and with associated molecular gas (Anderson et al. 2009). In addition to the usual absorption analysis, they searched for self-absorption by comparing the H I and ^{13}CO lines, where the signature of self-absorption is the presence of an H I absorption feature together with molecular emission at the same velocity.

In Table 1, we summarize the relevant results reported by Anderson & Bania (2009). In the area of G25.8700+0.1350, the authors identified five molecular clouds related to ionized gas, which are indicated by grey ellipses in Fig. 1 and described in Table 1. Column 2 gives the ID of the H II region related to each cloud as given by Anderson et al. (2009), while their Galactic coordinates are given in columns 3 and 4. Column 5 gives the radial velocity of the detected RRL. Columns 6 and 8 show the result (N, F or T) obtained according to each method, either the conventional H I absorption analysis (dubbed EA for emission/absorption) or the search for self-absorption (SA). Columns 7 and 9 give their corresponding quality parameters, where A and B stand, respectively, for high and low confidence of the results. Finally, the suggested distance is given in column 10. As can be seen in Fig. 1, clouds 1 and 2 are related to another H II region (catalogued as G25.7056+0.0389 by Helfand et al. 2006), while clouds 3, 4 and 5 are probably associated with G25.8700+0.1350, since they share both the radial velocity and spatial location. Note, however, that while regions 3 and 4 are put at the near distance, region 5 seems to be, although with less reliability, at the far side.

In summary, even though the distance to G25.8700+0.1350 has been estimated by many authors, there is no agreement in the different results they achieve. Since an accurate distance is crucial for determining the physical properties of the region, we will obtain our own estimate based on the available radio continuum and H I data.

3.1 Distance estimation

In the following, we study the H I absorption of G25.8700+0.1350 with the aim of constraining its systemic velocity and distance. For consistency, we convolved the 1420 MHz continuum image obtained from MAGPIS down to the resolution of the H I data. The on-source (T_{on}) absorption profile was obtained towards the brightest region of G25.8700+0.1350, which is enclosed by the radio continuum isophote at 600 mJy beam^{-1}. To obtain the expected H I profile at this region (T_{off}), we performed a bilinear fit using only the H I pixels within the yellow box in Fig. 2 outside the outer radio continuum contour, at 350 mJy beam^{-1}. The method (e.g. Reynoso, Cichowolski & Walsh 2017) consists in replacing those pixels within the inner contour by the average between two linear

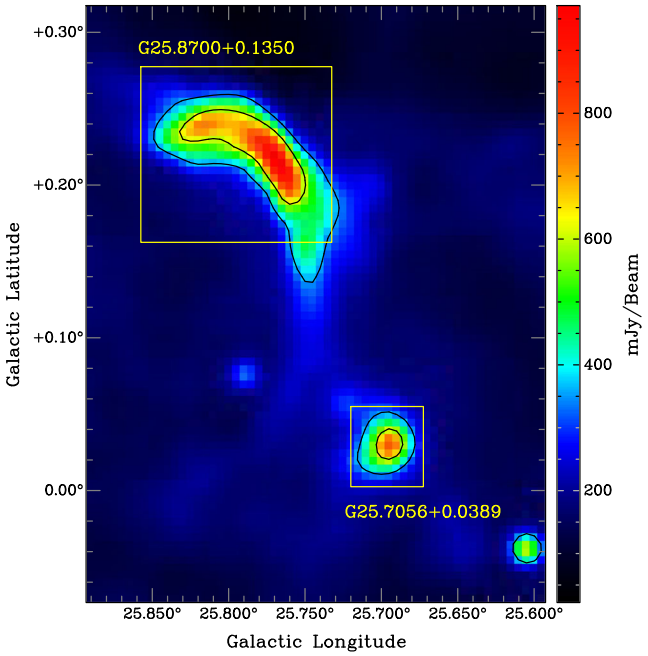

Figure 2. MAGPIS image of the region at 1420 MHz convolved to a 60 × 60 arcmin beam to match the resolution of the H I data. The intensity scale is displayed by a colour bar to the right. The two yellow boxes indicate the regions used to compute the absorption profiles towards G25.8700+0.1350 and G25.7056+00389, which are shown in Fig. 3. Black contours at 350 and 600 mJy beam^{-1} are plotted.

fits, one along the Galactic latitude and the other along the Galactic longitude. The result is shown by the blue solid line in Fig. 3. The absorption feature at the highest positive value appears at approximately +115 km s^{-1}. No absorption features are seen at negative values.

To facilitate the analysis of the H I absorption profile associated with G25.8700+0.1350, we followed the same method described above and obtained a second profile towards the bright nearby H II region G25.7056+00389. The result is displayed by the red solid lines in Fig. 3. A comparison between both profiles readily shows that although the H I emission level at approximately +125 km s^{-1} is the same for both sources, the red absorption profile contains a ∼10 km s^{-1}-wide feature, which is absent in the blue profile. We, thus, interpret that the last absorption feature towards G25.8700+0.1350 occurs before reaching the tangent point, and hence the region lies in the near side of the two possible distances associated with $v = +115$ km s^{-1}, 6.5 and 8.7 kpc, according to the Galactic rotation model of Fich, Blitz & Stark (1989). In the following, we will adopt a distance of 6.5 ± 1 kpc for G25.8700+0.1350.

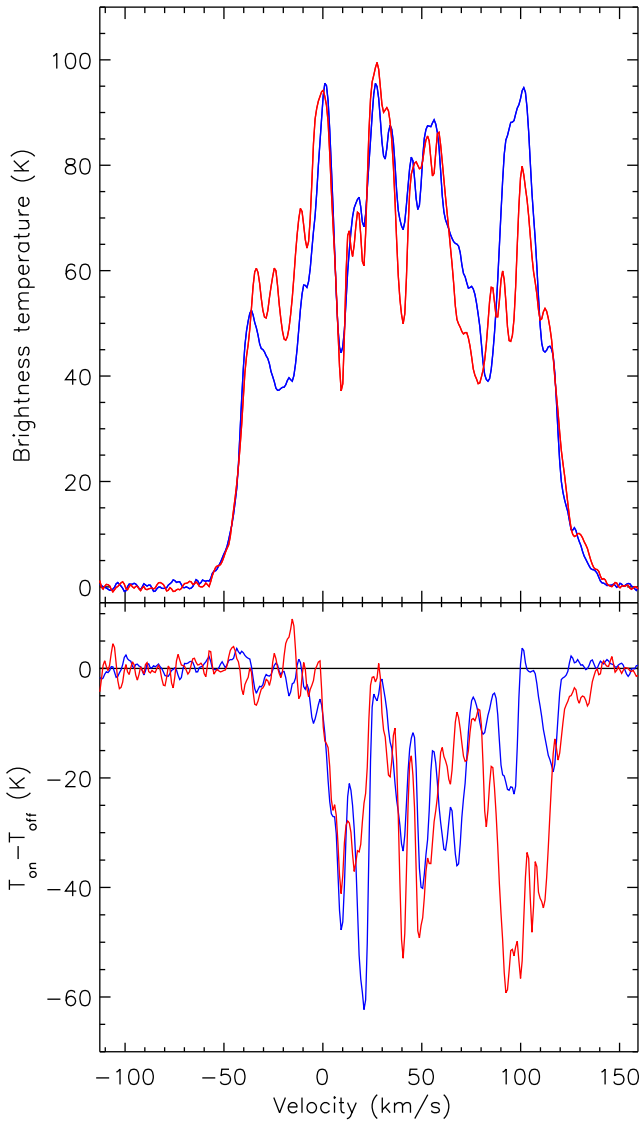

Figure 3. H I emission–absorption pairs towards G25.8700+0.1350 (blue lines) and G25.7056+00389 (red lines). Off-source H I profiles were computed by employing a bilinear fit, as explained in the text.

3.2 1420 MHz emission

3.2.1 Radio continuum

Fig. 1 clearly shows that G25.8700+0.1350 presents a very bright arc-shape structure superposed on to a faint, more extended emission. We estimated the average flux density of this emission to be 1.3 mJy beam^{-1}. Accounting for this background, we obtained that the total flux density of the bright arc is $S_{1420} = 12 \pm 1$ Jy, where the uncertainty includes the arbitrary assumptions used in determining the limits of the region.

We then estimated the physical parameters of G25.8700+0.1350 using the model developed by Mezger & Henderson (1967). We consider the spherical source model with an angular diameter of $\theta_{\rm sph} = 20$ arcmin and a filling factor of 0.08. Assuming our estimated distance value $D = 6.5 \pm 1.0$ kpc and the electron temperature inferred by Quireza et al. (2006b) $T_{\rm e} = 6120 \pm 100$ K, we obtain that the region has a mass of 2500 ± 1110 M$_\odot$ of ionized hydrogen and an electron density of $n_{\rm e} = 43 \pm 10$ cm^{-3}, which is similar to the value $n_{\rm e} = 45.7$ cm^{-3} obtained by Quireza et al. (2006b) using RRL data.

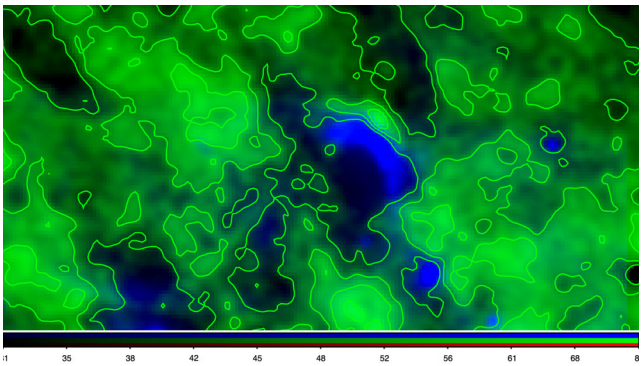

Figure 4. Green: H I emission distribution averaged over the velocity range from 109.8 to 118.1 km s^{-1}. Contour levels are at 40, 50, 60 and 70 K. Blue: Radio continuum emission at 1420 MHz.

Finally, we can estimate the number of UV photons necessary to keep the gas ionized, using the relation

$$N_{\rm UV} = 0.76\times10^{47} \left(\frac{T_{\rm e}}{10^4\,{\rm K}}\right)^{-0.45} \left(\frac{\nu}{\rm GHz}\right)^{0.1} \left(\frac{D}{\rm kpc}\right)^{2} \left(\frac{S_\nu}{\rm Jy}\right)\ {\rm s}^{-1}$$

(Chaisson 1976), which yields $N_{\rm UV} = (5.0 \pm 1.6) \times 10^{49}$ s^{-1} for G25.8700+0.1350.

3.2.2 H I line emission distribution

We inspected the H I emission distribution in the velocity range where the RRLs were observed and noticed two striking features in the velocity interval from 109.8 to 118.1 km s^{-1} (Fig. 4): (i) a conspicuous H I emission minimum around (l, b) = (25.8°, 0.2°) and (ii) a bright H I feature next to the arc-shaped structure detected in the radio continuum emission at 1420 MHz (see Section 3.2.1). Both features strongly suggest that the massive stars have ionized and probably swept up the surrounding ionized and neutral gas, generating an irregular cavity (Weaver et al. 1977). The morphology of G25.8700+0.1350 could be explained then as an H II region bounded by density towards higher Galactic longitudes, and bounded by ionization towards lower Galactic longitudes, probably as a result of the action of the powering stars over an inhomogeneously distributed original neutral gas. This scenario is in agreement with the morphology of the molecular gas component reported in the velocity range from 106.6 to 116.6 km s^{-1} towards higher Galactic longitudes, which is assumed to be related to the photodissociation region (PDR) (see Section 3.4).

It is important to mention, however, that an inspection of all the H I emission channels shows that there is no emission that could be interpreted as an approaching or receding cap. This absence may indicate either that the structure has a ring morphology or, as pointed out by Cazzolato & Pineault (2005), that there is significant velocity dispersion, making the receding and/or expanding caps hard to detect.

3.3 Infrared

At IR wavelengths, the region appears to be very conspicuous, as shown in Fig. 5. In fact, G25.8700+0.1350 was also identified in WISE images and catalogued as G025.867+00.118 (Anderson et al. 2014). Fig. 5 is a composite RGB image

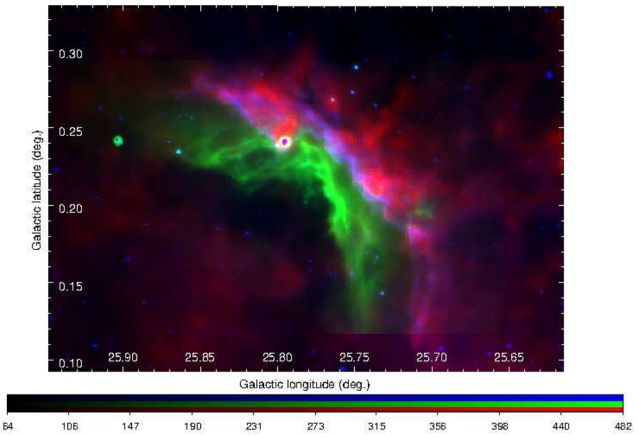

Figure 5. RGB image of G25.8700+0.1350 and surroundings. Red: Emission at 250 μm (*Herschel*). Green: Emission at 24 μm (*Spitzer*). Blue: Emission at 8 μm (*Spitzer*).

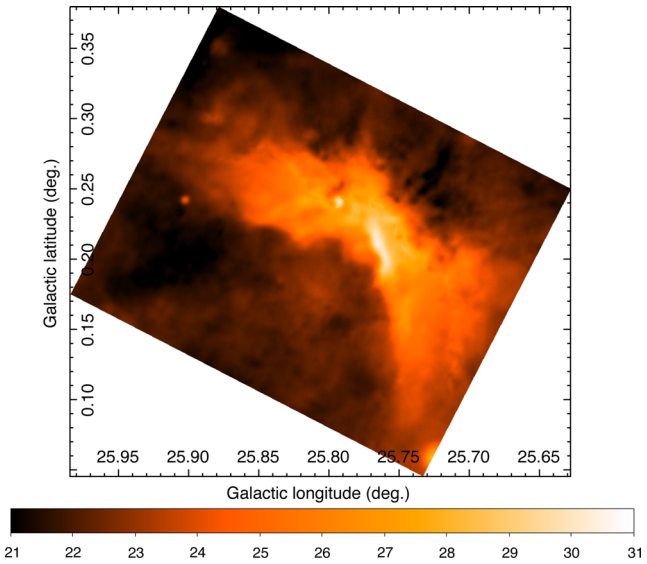

Figure 6. Colour temperature map based on emission at 70 and 160 μm. Colour bar units are expressed in kelvin.

of the region, where the emission at 250 μm, 24 μm and 8 μm is displayed in red, green and blue, respectively. Since the 8 μm emission mainly originates in the polycyclic aromatic hydrocarbons (PAHs), which are destroyed inside an H II region, this reveals the presence of a PDR (Hollenbach & Tielens 1997). The emission at 24 μm shows the dust heated by the energetic stellar photons while 250 μm data trace the emission from cold-dust big grains.

A remarkably strong source is readily observed at $(l, b) = (25.8^\circ, 0.24^\circ)$ in Fig. 5. This source, listed as G025.7961+00.2403 in the MSX catalogue, is classified as a compact H II region based on its IR colours. We will discuss its nature and possible origin in Section 4.2.

3.3.1 Dust temperature maps

Dust temperatures in the region were estimated using the emission at 70 and 160 μm. In a far-IR image, the dust temperature (T_d) in each pixel can be obtained by assuming that the dust in a single beam is isothermal and that the observed ratio of 70 to 160 μm is due to blackbody radiation from dust grains at T_d modified by a power-law emissivity. The method used to calculate the dust colour temperature is that used by Schnee et al. (2005). The 70 μm image was convolved to the resolution of the 160 μm image.

The flux density emission at a wavelength λ_i is given by

$$F_i = \frac{2hc}{\lambda_i^3 (e^{hc/(\lambda_i k T_d)} - 1)} N_d \alpha \lambda_i^{-\beta} \Omega_i, \quad (1)$$

where N_d represents the column density of dust grains, α is a constant that relates the flux to the dust optical depth, β is the emissivity spectral index and Ω_i is the solid angle subtended at λ_i by the detector.

Assuming that the dust emission is optically thin at 70 and 160 μm and that $\Omega_{70} \sim \Omega_{160}$, and adopting an index of $\beta = 2$, we can write the ratio R of the flux densities as

$$R = (0.4)^{-(\beta+3)} \frac{e^{90/T_d} - 1}{e^{205/T_d} - 1}. \quad (2)$$

The dust temperature T_d is derived from this equation. Fig. 6 shows the spatial distribution of the dust colour temperature, which varies from 20 to 31 K. The uncertainties were estimated to be about ∼10–15 per cent. The map shows a clear temperature gradient from the central regions (the inner arc-shaped structure, where the ionizing stars are located) to the periphery of the complex, while low temperatures (∼23 K) are measured at the location of the molecular clumps (see Section 3.4).

3.4 Millimetre and submillimetre emission

3.4.1 Carbon monoxide emission

In Fig. 7(a), we show the ^{13}CO(1-0) emission distribution map integrated within the velocity interval from 106.6 to 116.6 km s^{-1}. The molecular gas at this velocity interval has a partially arc-shaped structure, with the strongest emission coincident with the IR emission (see Section 3.3). This velocity interval is coincident with the velocity of the RRLs detected in the region (see Section 2). In (b), we show a composite image of the 8 μm emission with the ^{13}CO(1-0) emission. The molecular gas shows an excellent morphological correspondence with the IR emission, which indicates that this molecular component is being ionized by a stellar source (or sources) at lower Galactic longitudes, giving rise to a PDR. The strong H I emission almost between the radio continuum and the molecular emission (see Figs 4 and 1) suggests the existence of a central neutral gas layer between the ionized gas and the molecular gas, giving additional support to the PDR scenario. The molecular emission shows a sharp arc-shaped cut-off in the direction of the radio continuum emission while the intensity of the emission decreases smoothly towards the centre of the molecular cloud. This layout, which is indicative of a density gradient in the molecular distribution, suggests that the molecular gas has undergone ionization and has probably been compressed on the front side as a result of the expansion of the ionization front and/or by the action of winds of the powering star(s). The incomplete shell structure of the molecular component and the location of the brightest molecular emission (behind the radio continuum emission at 1420 MHz) give further support to the previously proposed scenario of an H II region density-bounded towards higher Galactic longitudes and ionization bounded towards lower Galactic longitudes. In Fig. 7(c), we show the CO(3-2) emission distribution in the region, which has a similar feature.

It is clear from Fig. 7 that the molecular emission is not uniformly distributed and several clumps can be distinguished in the brightest region next to the ionization front. From the present data, it is

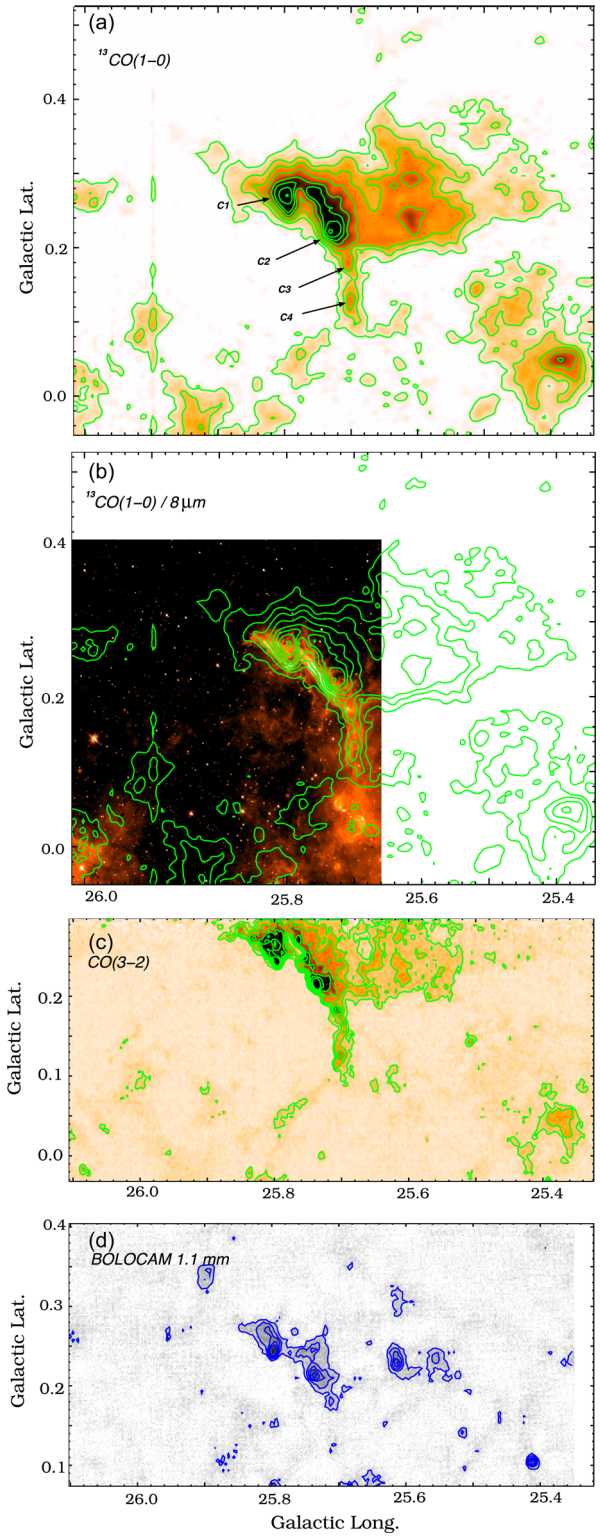

Figure 7. (a) ^{13}CO(1-0) emission map in the velocity range from 106.6 to 116.6 km s^{-1}. Contour levels start from 0.2 K km s^{-1} with a contour spacing of 0.2 K km s^{-1}. The positions of molecular clumps C1 and C2 are indicated (see text). (b) Composite image showing the emission of the ^{13}CO(1-0) line (green contours) over the *Spitzer* 8 μm emission (red). (c) CO(3-2) emission map in the velocity range from 106.6 to 116.6 km s^{-1}. Contour levels start from 1 K km s^{-1} with a contour spacing of 1 K km s^{-1}. (d) Bolocam 1.1 mm emission. Contour levels start from 100 mJy beam^{-1} ($\sim 3\sigma$) with a contour spacing of 100 mJy beam^{-1}.

difficult to ascertain whether these clumps are pre-existing concentrations in the molecular structure or instead whether they formed by the accumulation of molecular gas due to the expansion of the ionization front and/or the action of stellar winds. Observational evidence (see previous paragraph) suggests the latter scenario, although the cometary shape of C1 in the continuum emission at 1.1 mm (see Section 3.4.2) might indicate that this clump formed earlier.

The physical properties of these clumps must be estimated if a study of the molecular gas is intended. In the following analysis, we will concentrate only on the molecular clumps located along the PDR, which very likely were formed by the expansion of the ionized gas over the parental molecular cloud. These clumps will hereafter be dubbed as clumps C1, C2, C3 and C4. It is worth pointing out that clumps C1 and C2 were identified by Anderson & Bania (2009) as the molecular components of U25.80+0.24 and C25.77+0.21, respectively. The location and size of clump C1 is coincident with the MSX source G025.7961+00.2403 and the bright IR source reported at 8, 24 and 250 μm in Section 3.3 (see Fig. 5).

In Table 2, we present some physical properties derived for the CO clumps. We define the area of each clump ($A_{\rm clump}$, column 2) by the contour level corresponding to half the ^{13}CO peak emission ($T^{13}_{\rm peak}$, column 5). The optical depth of the ^{13}CO emission (τ^{13}, column 7) and the ^{13}CO column density ($N(^{13}{\rm CO})$) were calculated from

$$\tau^{13} = -\ln\left(1 - \frac{T^{13}_{\rm peak}}{5.29J[T_{\rm exc}] - 0.164}\right) \qquad (3)$$

and

$$N(^{13}{\rm CO}) = 2.42\times10^{14}\tau^{13}\frac{\Delta v T_{\rm exc}}{1-e^{(-5.29/T_{\rm exc})}}, \quad ({\rm cm}^{-2}) \qquad (4)$$

where $J[T({\rm K})] = 1/(e^{5.29/T({\rm K})}-1)$, Δv is the full width at half-maximum line width and $T_{\rm exc}$ is the excitation temperature of the $J = 1 \rightarrow 0$ transition of the ^{13}CO (column 6). The excitation temperature is usually estimated by the peak temperature of the optically thick CO(1-0) emission, through the equation

$$T_{\rm exc} = \frac{5.53}{\ln[1 + 5.53/(T_{\rm peak}({\rm CO}) + 0.819)]}. \quad ({\rm K}) \qquad (5)$$

Since no CO(1-0) line data with spatial resolution better than $\sim$9 arcmin is available for this quadrant of the Galaxy (Dame, Hartmann & Thaddeus 2001), we made use of the empirical relation

$$T_{\rm peak}({\rm CO}(1-0)) = \frac{T_{\rm peak}({\rm CO}(3-2)) + 0.222}{0.816} \qquad (6)$$

derived by Oka et al. (2012) for the Galactic centre. Then, the H_2 column density ($N(H_2)$, column 8) was derived using $N(H_2)/N(^{13}{\rm CO}) = 5\times10^5$ (Dickman 1978). The peak optical depth ($\tau^{13}_{\rm peak}$) and peak column density ($N(H_2)_{\rm peak}$) are indicated in columns 9 and 10, respectively.

The molecular mass was calculated using

$$M(H_2) = (m_{\rm sun})^{-1}\mu m_{\rm H}\sum A_{\rm clump}N(H_2)d^2, \quad ({\rm M}_\odot) \qquad (7)$$

where $m_{\rm sun}$ is the solar mass ($\sim 2\times10^{33}$ g), μ is the mean molecular weight, which is assumed to be equal to 2.8 to allow for a relative helium abundance of 25 per cent, $m_{\rm H}$ is the hydrogen atom mass ($\sim 1.67\times10^{-24}$ g) and d is the distance (estimated to be 6.5 kpc; Section 3.1). The volume density ($n_{\rm H_2}$, column 12) was estimated

Table 2. Physical properties derived for the CO clumps.

	$A_{\rm clump}$ (10^{-6} sr)	$R_{\rm eff}$ (10^{19} cm)	$V_{\rm LSR}$ (km s^{-1})	$T^{13}_{\rm peak}$ (K)	$T_{\rm exc}$ (K)	τ^{13}	$N(H_2)$ (10^{22} cm^{-2})	$\tau^{13}_{\rm peak}$	$N(H_2)_{\rm peak}$ (10^{22} cm^{-2})	M_{H_2} (10^4 M$_\odot$)	n_{H_2} (10^3 cm^{-3})	$N_{\rm int}(H_2)$ (10^{22} cm^{-2})	$M_{\rm int}$ (10^4 M$_\odot$)
C1	0.98	1.12	110.3	7.9	46.5	0.06	3.2	0.19	9.9	2.8	2.1	2.6	0.8
C2	2.05	1.62	110.6	8.1	32.1	0.08	2.0	0.31	7.9	3.6	0.9	2.3	1.1
C3	0.23	0.54	111.6	4.8	24.8	0.05	0.8	0.24	3.7	0.16	1.1	1.1	0.3
C4	0.83	1.03	111.7	4.4	16.5	0.12	0.9	0.42	3.1	0.31	0.3	0.9	0.3

considering spherical geometry, as

$$n_{H_2} = \frac{M_{H_2}}{4/3\pi\, R_{\rm eff}^3 \mu m_{\rm H}}, \quad (8)$$

where $R_{\rm eff}$ (column 3) is the effective radius of the clump, estimated as $R_{\rm eff} = \sqrt{A_{\rm clump}/\pi}$.

A different approach for estimating the column density uses the CO(3-2) integrated intensity emission:

$$N_{\rm int}(H_2) = X \times \int \frac{T({\rm CO}(3-2))\,{\rm d}v}{0.7}, \quad (9)$$

where X is an empirical factor that has been shown to be roughly constant for Galactic molecular clouds. For the ^{12}CO(1-0) line, the X value is about 1.9×10^{20} K km s^{-1} (Strong & Mattox 1996). Since we use the integrated intensity emission of the CO(3-2) line, we need to adjust the value of $N_{\rm int}(H_2)$ using a correction factor of ∼0.7 (Oka et al. 2012). Hence, the integrated mass ($M_{\rm int}$) is calculated using equations (7) and (9).

3.4.2 *Continuum 1.1 mm emission*

The continuum emission at 1.1 mm is usually dominated by optically thin thermal emission from cold dust embedded in dense material (e.g. dense star-forming cores or clumps and filaments), turning this emission into one of the most reliable tracers of dense molecular gas.

In Fig. 7(d), we show a 1.1 mm continuum emission image obtained from the Bolocam survey. As expected, the emission appears concentrated towards the position of the PDR. Three bright structures can be discerned coincident with the CO clumps C1, C2 and C3. For clarity, we will also refer to these structures as C1, C2 and C3. C1 and C2 were identified as G025.797+00.245 and G025.737+00.213, respectively, in the catalogue of Bolocam Galactic Plane Survey sources (Shirley et al. 2013). The presence and location of these submillimetre sources along the border of the H II region is further confirmation of the existence of high-density molecular gas, which probably accumulated due to the expansion of the ionization front over the molecular environment. This makes clumps C1, C2 and C3 excellent candidates to search for star formation activity. C1 deserves a special mention. Its cometary shape suggests the existence of a pre-existing molecular clump where an ionized boundary layer (IBL) produced by nearby O-type stars may be acting to induce the gravitational collapse. Triggered star formation scenarios will be further tested for the regions C1, C2 and C3 (see Section 4.2.2).

We estimated the total (H_2 + dust) mass of C1, C2 and C3 from their integrated 1.1 mm emission, assuming that the emission is optically thin, and using the equation of Hildebrand (1983):

$$M_{\rm (tot)} = R \frac{S_{1.1\,{\rm mm}} d^2}{\kappa_{1.1\,{\rm mm}} B_{1.1\,{\rm mm}}(T_{\rm dust})}, \quad (10)$$

where R is the gas-to-dust ratio, assumed to be 186 (Draine et al. 2007), $S_{1.1\,{\rm mm}}$ is the flux density, d is the distance (6.5 kpc), $\kappa_{1.1\,{\rm mm}}$ is the dust opacity per unit mass at 1.1 mm assumed to be 1.0 cm^2 g^{-1} (estimated for dust grains with thin ice mantles in cold clumps; Ossenkopf & Henning 1994) and $B_{1.1\,{\rm mm}}(T_{\rm dust})$ is the Planck function for temperature $T_{\rm dust}$. The beam-averaged column densities (N_{H_2}) of sources C1, C2 and C3 were calculated using

$$N_{H_2} = R \frac{I_{\rm peak}}{\Omega_{\rm beam}\kappa_{1.1\,{\rm mm}}\mu\, m_{\rm H} B_{1.1\,{\rm mm}}(T_{\rm dust})}, \quad (11)$$

where $I_{\rm peak}$ is the 1.1 mm continuum emission peak intensity, $\Omega_{\rm beam}$ is the beam solid angle ($\pi\theta^2_{\rm HPBW}/4\ln(2)$), μ is the mean molecular weight (assumed to be 2.8 considering a relative helium abundance of 25 per cent) and $m_{\rm H}$ is the mass of the hydrogen atom.

Table 3. Parameters derived from the Bolocam 1.1 mm emission.

	$T_{\rm dust}$ (K)	$M_{\rm (tot)}$ (10^4 M$_\odot$)	N_{H_2} (10^{22} cm^{-2})
C1	25.4	2.8	3.5
C2	24.0	3.4	2.6
C3	25.6	0.02	1.1

The estimated masses, column densities and dust temperature used for the calculations (obtained from Fig. 6), are listed in Table 3. A direct comparison between Tables 2 and 3 shows there is good agreement in masses and densities for C1 and C2. A discrepancy, nonetheless, is observed in the estimated masses for C3, very likely due to uncertainties in the estimation of the clump boundaries.

4 DISCUSSION

4.1 Origin of the structure

In this section, we attempt to find the stars responsible for the origin of G25.8700+0.1350. Considering that early-type high-mass stars are very important in perturbing the ISM, we searched for such stars in the whole area by inspecting every catalogue available, but we obtained negative results. The paucity of candidate stars can be explained by the high absorption of the intervening gas and dust column up to a distance of 6.5 kpc, which can make even bright early-type stars hard to detect. Taking into account that the extinction in the visual band is of the order of 1.8 mag kpc^{-1} near the Galactic plane (Whittet 2003), the visual absorption for a distance of 6.5 ± 1.0 kpc would be between 10 and 13.5 mag.

Another estimate for the visual absorption A_V can be inferred using the Galactic extinction model developed by Chen et al. (1999). For positive Galactic latitudes, they propose the relation

$$\frac{E(B-V)(D,l,b)}{E(B-V)(\infty,l,b)} = 1 - \exp\left(-\frac{D\sin b}{h}\right),$$

where $E(B-V)(\infty, l, b)$ is the total reddening in the line of sight ($D = \infty$), and h is the scale height of the Galactic plane absorbing dust, $h = 117.7 \pm 4.7$ pc (Kos et al. 2014). To apply this

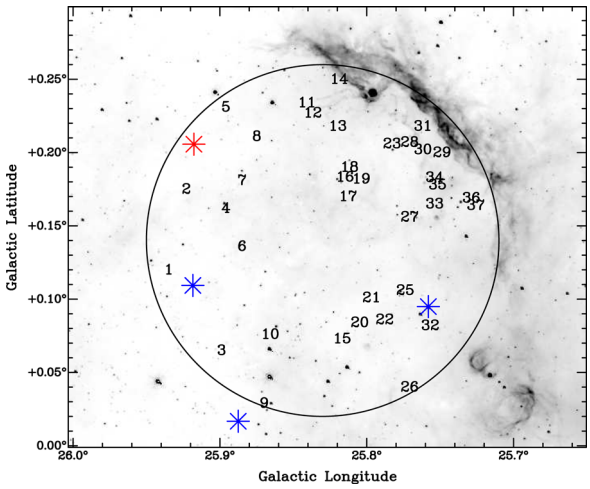

Figure 8. *Spitzer* emission at 8 μm. The circle shows the region considered in the search for the exciting stars. The red asterisk indicates the location of the WR star HDM 40, while the numbers correspond to the IDs of the 2MASS sources given in the first column of Table 5. The blue asterisks show the location of the three RSGs in the region.

procedure, we first inspected the IR emission distribution in the region of G25.8700+0.1350 to identify the region where the exciting stars are more probably located. The H II region has an arc-like shape; hence, the exciting stars are expected to appear near its centre of curvature. In Fig. 8 the region used to look for the ionizing stars is indicated. The value of $E(V-B)(\infty, l, b)$ was obtained using the dust map of the Galaxy constructed by Schlafly & Finkbeiner (2011). Assuming $A_V = 3.1E(B-V)$, we estimated that the visual absorption in the region is between 10 and 16 mag. This high extinction can explain why the ionized region, being very bright in the radio continuum, is not visible at optical wavelengths, and implies that any candidate early-type ionizing star(s) must be searched for in IR wavelengths.

Several Wolf–Rayet (WR) stars have been recently identified in the IR by Mauerhan, Van Dyk & Morris (2011). Among them, there is one located at $(l, b) = (25.92^\circ, 0.21^\circ)$ (red asterisk in Fig. 8), which could be related to G25.8700+0.1350. This object is the 2MASS source 18375149-0608417 and was identified as HDM 40 and classified as a WC9d star, since strong evidence has been found of associated thermal dust emission. Mauerhan et al. (2011) estimated for HDM 40 a photometric distance of 4.9 kpc, with an uncertainty probably up to 25–40 per cent. The authors claim, however, that this distance should be taken with caution, since the probable thermal dust emission from this star can make the adopted colours and K_s-band absolute photometry not reliable.

RSGs can be used to trace recent high-mass star formation even in heavily obscured regions. These high-mass stars are young (between 8 and 25 Myr; Ekström et al. 2013) and very luminous (from $10^{4.5}$ to $10^{5.8}$ $L_\odot$). However, unlike ionizing high-mass stars, RSGs present late spectral types (K and, mostly, M) and red colours. Therefore, they are significantly brighter in IR bands, and they are more accessible targets for spectroscopic surveys in such bands. In consequence, RSGs are a powerful tool for studying highly extinguished high-mass populations. There are two large high-mass clusters close to G25.8700+0.1350: RSGC1 ($l = 25.27^\circ$, $b = -0.16^\circ$; Figer et al. 2006; Davies et al. 2008) and RSGC2 ($l = 26.19^\circ$, $b = -0.07^\circ$; Davies et al. 2007). Due to their high extinction (between 11 and 26 mag in V), the only stellar components observable in them are RSGs. These two clusters have radial velocities (123.0 ± 1.0 and 109.3 ± 0.7 km s^{-1}, respectively) and, thus, kinematic distances compatible with G25.8700+0.1350 (6.6 ± 0.9 and $5.8^{+1.9}_{-0.8}$ kpc, respectively). Given their high initial masses (30 ± 10 $M_\odot$ and 40 ± 10 $M_\odot$), estimated through population synthesis models from their current RSG population, they should have hosted a significant number of O stars. However, given that the clusters have ages of 12 ± 2 and 17 ± 3 Myr, largely exceeding the typical lifetimes of O-type stars, such stars are not expected to exist currently in the clusters. Thus, these clusters are necessarily older than G25.8700+0.1350, for which a significant number of O stars is required to explain its radio continuum emission.

Despite the difference in age between the clusters and G25.8700+0.1350, it is not unlikely that G25.8700+0.1350 may be related somehow to these clusters. It has been determined that these clusters are part of an extended stellar association (Negueruela et al. 2012), as there is an overdensity of RSGs around them having compatible radial velocities, which is indicative of intense high-mass star-forming activity in the region. In fact, the centre of G25.8700+0.1350 is between RSGC1 and RSGC2 (see Fig. 9). It is separated from them by 39.8 and 22.6 arcmin, respectively. At the estimated distance of G25.8700+0.1350, 6.5 ± 1 kpc, these separations correspond to *minimum* physical distances of 75^{+12}_{-11} and 43^{+6}_{-7} pc. Moreover, G25.8700+0.1350 has a radius of about 8.5 arcmin (16 pc). Therefore, the edges of G25.8700+0.1350 are even closer to these clusters. Considering that both clusters are separated by 54.6 arcmin (103 pc at the distance of G25.8700+0.1350) and since they seem to belong to the same association, it is unlikely that a high-mass star-forming region like G25.8700+0.1350 is not related to them and to the overdensity of RSGs around them. Moreover, the age difference between the clusters (5 Myr) is not much shorter than the difference that we should expect between RSGC1 and the O stars in G25.8700+0.1350 (8–9 Myr). Therefore, we suggest that G25.8700+0.1350 may represent the youngest star-forming burst of this high-mass star association.

According to evolutionary models (Ekström et al. 2013), only those RSGs of higher masses and luminosities come from the evolution of O stars. Thus, the presence of RSGs related to G25.8700+0.1350 may provide hints about its past O-star population history. Given the overdensity of RSGs in this region, we searched for RSGs lying close to G25.8700+0.1350 in the spectroscopic catalogue of Dorda et al. (in preparation). This catalogue provides spectral classifications as well as radial velocities for the stars observed (Dorda et al. 2016). We found three RSGs in the area of G25.8700+0.1350 with compatible radial velocities (see Table 4 and Fig. 8). We used their spectral types together with the work of Levesque et al. (2005) to estimate $(J-K_s)_0$. Then we calculated $E(J-K_s)$ using the 2MASS photometry and we dereddened k_s applying the calibration of Rieke & Lebofsky (1985). We also calculated the bolometric magnitude, using the bolometric corrections proposed by Levesque et al. (2005). Finally, considering that we want to evaluate whether these RSGs are related to G25.8700+0.1350, we used the distance to this H II region to calculate their absolute magnitudes. The masses and the corresponding age interval of the RSGs were roughly estimated through M_{bol}, since evolutionary models predict that the luminosity of an RSG depends strongly on its initial mass. For this estimation, we used the evolutionary tracks of Geneva (Ekström et al. 2012). Under the distance assumed, RSGs 2 and 3 are too faint to have evolved from O stars, and thus, they are too old to be related in any way to G25.8700+0.1350. However, for RSG 1, with $M_{bol} \sim -8$, we estimate $M_i \sim 20\,M_\odot$, which may well imply a late O-star origin

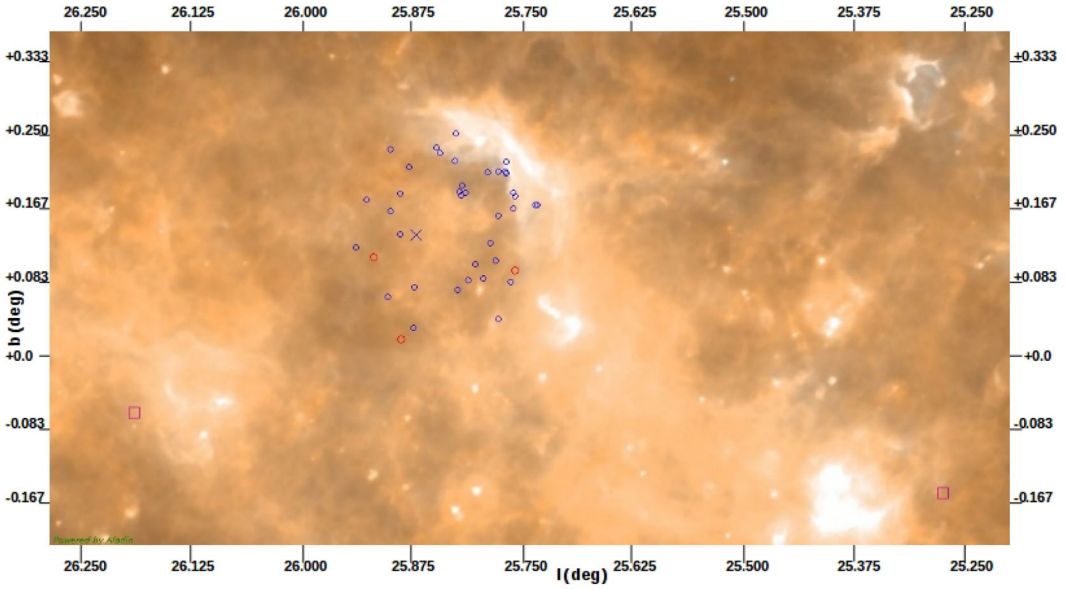

Figure 9. Two-colour composite image of G25.8700+0.1350 and its surroundings. Blue: PACS 70 μm. Red: PACS 160 μm. The OV source candidates and the RSGs known in the region are represented by blue and red circles, respectively. The blue cross indicates the location of the centre of G25.8700+0.1350, and the squares the position of the RSG clusters, RSGC1 and RSGC2.

Table 4. RSGs from Dorda et al. (2016) in the area of G25.8700+0.1350 and with compatible radial velocities.

ID	2MASS source	l (°)	b (°)	$V_{\rm LSR} \pm 1$ (km s^{-1})[a]	Spectral type[a]	K (mag)[b]	$M_{\rm bol}$ (mag)[b]
1	18375756-0620155	025.75802	+00.09493	97	M2.5	−10.77	−7.94
2	18382868-0615304	025.88752	+00.01671	103	M3.5	−8.15	−5.27
3	18381223-0611186	025.91842	+00.10935	101	M2	−10.26	−7.46

Notes. [a]Spectral type and $V_{\rm LSR}$ are averaged values from the multiple epochs available.
[b]The absolute magnitudes were calculated assuming the distance of G25.8700+0.1350, 6.5 kpc.

(O8V–O9V). An RSG having such a mass should have an age between 8 and 9 Myr, which implies that all but the latest O stars have already died if coeval, and thus it should be related to a population whose the most massive members at present are O9V stars. In consequence, to confirm the relation between RSG 1 and G25.8700+0.1350, it is necessary to know the spectral types and radial velocities of the early-type high-mass stars in this region.

Bearing in mind that early-type high-mass stars have a huge impact on the surrounding gas via their high rate of energetic photons and stellar winds, the presence of cavities, shells and H II regions can be used as good tracers for their existence. Thus, as mentioned above, taking into account the morphology of G25.8700+0.1350, we constrained the region where the exciting stars are most probably located (see Fig. 8) and looked for exciting star candidates using the 2MASS source catalogue (Cutri et al. 2003). We selected the candidates using the IR reddening-free pseudo-colour $Q_{\rm IR} = (J - H) - 1.83(H - K_{\rm s})$, picking those 2MASS sources with $-0.15 < Q_{\rm IR} < 0.1$, indicative of main sequence stars (Comerón et al. 2002).

We found 1764 sources inside the region having the best photometric quality (ph-qual = AAA) in the three bands J (1.235 μm), H (1.662 μm) and $K_{\rm s}$ (2.159 μm). Among them, 262 are classified as main sequence star candidates. Fig. 10 shows a colour–colour diagram depicting the distribution of all sources, with the main sequence ones plotted in blue. The figure also shows the positions of the dereddened main sequence and giant stars. We located the

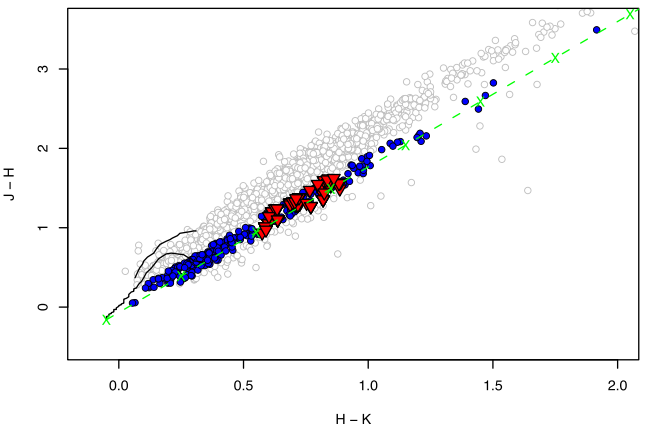

Figure 10. Colour-colour diagram of the 2MASS sources projected on to the region shown in Fig. 8. Main sequence candidates are plotted with blue circles. The positions of the dereddened early-type main sequence and giant stars are shown by black lines. The reddening vector for O9 V stars (dashed green line) is indicated. The OV source candidates to be related to G25.8700+0.1350 are represented by red triangles.

O stars in the main sequence using the values given by Martins & Plez (2006), and those given by Tokunaga (2000) and Drilling & Landolt (2000) for late-type stars (B to M). The reddening vector for an early-type (O9V) star is represented by a dashed green line

Table 5. Parameters of exciting star candidates.

ID	2MASS source	l (°)	b (°)	J (mag)	H (mag)	K_s (mag)	$M_J^{(a)}$ (mag)	$M_H^{(a)}$ (mag)	$M_K^{(a)}$ (mag)
1	18381209-0609575	25.938	0.12	15.087	13.497	12.662	−1.78/−3.46	−2.27/−3.29	−2.50/−3.16
2	18375910-0609061	25.926	0.175	14.589	13.298	12.611	−2.28/−3.96	−2.47/−3.49	−2.55/−3.21
3	18381995-0613242	25.902	0.065	14.72	13.409	12.656	−2.14/−3.82	−2.36/−3.38	−2.51/−3.17
4	18375890-0610528	25.899	0.162	13.817	12.803	12.217	−3.05/−4.73	−2.96/−3.98	−2.95/−3.61
5	18374388-0609002	25.899	0.231	14.328	13.185	12.583	−2.54/−4.22	−2.58/−3.60	−2.58/−3.24
6	18380328-0612113	25.888	0.136	13.141	11.939	11.325	−3.72/−5.40	−3.83/−4.85	−3.84/−4.50
7	18375349-0610555	25.888	0.181	13.54	12.214	11.508	−3.32/−5.00	−3.55/−4.57	−3.66/−4.32
8	18374590-0610389	25.878	0.211	13.664	12.286	11.564	−3.20/−4.88	−3.48/−4.50	−3.60/−4.26
9	18382436-0615561	25.873	0.029	14.888	13.318	12.429	−1.98/−3.66	−2.45/−3.47	−2.74/−3.40
10	18381429-0614414	25.872	0.076	14.964	13.358	12.522	−1.90/−3.58	−2.41/−3.43	−2.64/−3.30
11	18373768-0611408	25.847	0.234	14.287	12.69	11.868	−2.58/−4.26	−3.07/−4.09	−3.30/−3.96
12	18373856-0612053	25.843	0.227	14.89	13.341	12.543	−1.97/−3.65	−2.42/−3.44	−2.62/−3.28
13	18373870-0613133	25.826	0.218	13.759	12.657	12.02	−3.11/−4.79	−3.11/−4.13	−3.14/−3.80
14	18373172-0612247	25.825	0.25	14.141	13.205	12.63	−2.72/−4.40	−2.56/−3.58	−2.53/−3.19
15	18380952-0617237	25.823	0.073	13.026	11.741	11.029	−3.84/−5.52	−4.02/−5.04	−4.14/−4.80
16	18374551-0614256	25.821	0.184	13.46	12.137	11.44	−3.40/−5.08	−3.63/−4.65	−3.72/−4.38
17	18374618-0614401	25.819	0.18	13.48	12.24	11.605	−3.38/−5.06	−3.52/−4.54	−3.56/−4.22
18	18374373-0614273	25.818	0.19	14.679	13.119	12.281	−2.19/−3.87	−2.65/−3.67	−2.88/−3.54
19	18374508-0614503	25.814	0.182	13.949	12.593	11.774	−2.92/−4.60	−3.17/−4.19	−3.39/−4.05
20	18380578-0617446	25.811	0.084	14.849	13.225	12.363	−2.02/−3.70	−2.54/−3.56	−2.80/−3.46
21	18380121-0617407	25.803	0.101	14.098	12.539	11.656	−2.77/−4.45	−3.23/−4.25	−3.51/−4.17
22	18380355-0618358	25.794	0.086	14.121	13.148	12.558	−2.74/−4.42	−2.62/−3.64	−2.61/−3.27
23	18373718-0615341	25.789	0.206	14.584	13.051	12.202	−2.28/−3.96	−2.71/−3.73	−2.96/−3.62
24	18375398-0617554	25.786	0.126	14.725	13.284	12.46	−2.14/−3.82	−2.48/−3.50	−2.70/−3.36
25	18375763-0618478	25.78	0.106	13.171	11.859	11.173	−3.69/−5.37	−3.91/−4.93	−3.99/−4.65
26	18381156-0620453	25.777	0.04	14.281	13.011	12.241	−2.58/−4.26	−2.75/−3.77	−2.92/−3.58
27	18374651-0617334	25.777	0.156	14.933	13.454	12.646	−1.93/−3.61	−2.31/−3.33	−2.52/−3.18
28	18373564-0616112	25.777	0.207	14.042	12.755	12.037	−2.82/−4.50	−3.01/−4.03	−3.13/−3.79
29	18373488-0616374	25.769	0.206	15.011	13.52	12.634	−1.85/−3.53	−2.24/−3.26	−2.53/−3.19
30	18373506-0616423	25.768	0.205	15.061	13.442	12.602	−1.80/−3.48	−2.32/−3.34	−2.56/−3.22
31	18373224-0616205	25.768	0.218	14.87	13.396	12.63	−1.99/−3.67	−2.37/−3.39	−2.53/−3.19
32	18380088-0620213	25.763	0.082	14.748	13.379	12.668	−2.12/−3.80	−2.39/−3.41	−2.50/−3.16
33	18374279-0618120	25.76	0.165	14.225	12.926	12.202	−2.64/−4.32	−2.84/−3.86	−2.96/−3.62
34	18373904-0617427	25.76	0.183	13.459	12.405	11.805	−3.41/−5.09	−3.36/−4.38	−3.36/−4.02
35	18373971-0617559	25.758	0.179	14.253	13.015	12.388	−2.61/−4.29	−2.75/−3.77	−2.78/−3.44
36	18373913-0619269	25.735	0.169	12.574	11.413	10.804	−4.29/−5.97	−4.35/−5.37	−4.36/−5.02
37	18373896-0619328	25.733	0.169	14.959	13.467	12.662	−1.91/−3.59	−2.30/−3.32	−2.50/−3.16

Note. *Absolute magnitudes estimated for $D = 6.5$ kpc and $A_v = 10/16$ mag.

using extinction values from Rieke & Lebofsky (1985). From Fig. 10, we selected the main sequence candidates lying along the reddening vector between $A_V = 10$ and 16 mag and computed their M_J, M_H and M_K absolute magnitudes, assuming a distance of $D = 6.5 \pm 1.0$ kpc. We then analysed whether the estimated magnitudes are in agreement with the absolute magnitudes of O-type stars given by Martins & Plez (2006). From this comparison, we finally found that 37 out of the 1764 2MASS sources could be O-type stars related to G25.8700+0.1350. They are listed in Table 5, indicated by red triangles in Fig. 10 and by numbers in Fig. 8.

An inspection of their estimated absolute magnitudes (see columns 8, 9 and 10 of Table 5) shows that several of them could be brighter than an O9V-type star, for which $M_J = -3.48$, $M_H = -3.38$ and $M_K = -3.28$ mag (Martins & Plez 2006), thus suggesting that more than one episode of massive stellar formation has taken place during the last million years.

It is important to note that these 37 sources are just candidates for being responsible for the ionized region, and to confirm this association, it is necessary to analyse their spectra. Besides, given the several assumptions involved in the method used to select the O-type star candidates, a certain degree of contamination is to be expected. To estimate the possible contamination level, we applied the same method to a nearby region, covering the same area but centred at $(l, b) = (26.0°, 0.295°)$. We found that 19 out of 1464 2MASS sources (with AAA quality) are OV star candidates (at a distance of 6.5 kpc and with A_V between 10 and 16 mag), which is about half the number we found in the G25.8700+0.1350 region, suggesting that there are probably less than 19 unrelated objects.

As mentioned in Section 3.2.1, the number of ionizing photons needed to keep the region ionized is very high, $N_{UV} = (5.0 \pm 1.6) \times 10^{49}$ s^{-1}. This number of UV photons could be supplied by several early-type stars, like three O5V, 12 O7V or 63 O9V stars (Martins, Schaerer & Hillier 2005). Moreover, since in the estimation of N_{UV} the effect of the dust is not taken into account, these figures are just lower limits. In this context, we conclude that most of the 37 2MASS sources found as O-type star candidates could indeed be related to G25.8700+0.1350. Finally, the presence of at least one supergiant suggests that there have been several supernovae in the area. The absence of catalogued supernova remnants within this region could be explained if the explosions occurred $\gtrsim 10^5$ yr ago and the remnants have dissipated into the ISM or if the putative supernova remnants are confused

with line-of-sight emission from other sources along this complicated direction of the Galaxy, towards the Galactic plane. However, although not detected directly, shock waves driven by past supernova explosions must have contributed to shape the ISM and could explain the asymmetry of the shell displayed by G25.8700+0.1350.

4.2 Star formation activity in the region

In the following, we will study if recent star formation activity has taken place in the vicinity of G25.8700+0.1350 to disentangle whether the seemingly expanding motion of the H II region could have triggered star formation. For this purpose, we will try to detect all young stellar object candidates (cYSOs) around the region and analyse their position with respect to the ionized gas and to the molecular condensations.

4.2.1 Identification of young stellar object candidates

The primary tracers of stellar formation activity were searched for using the MSX Infrared Point Source Catalogue (Egan, Price & Kraemer 2003), the WISE All-Sky Source Catalogue (Wright et al. 2010) and the GLIMPSE point source catalogue (Benjamin et al. 2003). MSX sources were selected if their variability and reliability flags were 0 and the flux quality Q was above 1 in all four bands. WISE sources with photometric flux uncertainties above 0.2 mag and signal-to-noise ratio lower than 7 in the $W1$, $W2$ and $W3$ bands were rejected. Finally, *Spitzer* sources were kept if their photometric uncertainties were lower than 0.2 mag in all four IRAC bands.

Within a 9-arcmin radius circle centred at $(l, b) = (25.83^\circ, 0.18^\circ)$, a total of three MSX, 511 WISE and 1716 *Spitzer* sources have been found fulfilling the selection criteria above. To identify the cYSOs among these sources, we adopted the classification scheme described in Lumsden et al. (2002), Koenig et al. (2012) and Gutermuth et al. (2009) for the MSX, WISE and IRAC data, respectively. Several sources were found to qualify as cYSOs, and are listed in Table 6. The IR colours of MSX sources permit us to discern between high-mass cYSOs and compact H II region (CHII) candidates (Lumsden et al. 2002). Two of the MSX sources selected in this region belong to this latter class.

Before attempting to identify the cYSOs from the listed WISE and *Spitzer* sources, we selected the non-YSO sources with excess IR emission, such as PAH-emitting galaxies, broad-line active galactic nuclei, unresolved knots of shock emission and PAH-emission features. A total of 67 and 132 WISE and *Spitzer* sources, respectively, were dropped from the lists. Among the remaining 444 WISE and 1584 *Spitzer* sources, 13 (four WISE and nine *Spitzer*) were identified as class I sources (i.e. sources where the IR emission arises mainly from a dense infalling envelope, including flat spectrum objects) and 63 (56 WISE and 16 Spitzer) as class II sources (i.e. pre-main sequence stars with optically thick discs).

For the WISE sources identified as cYSOs, we discarded those not compatible with T Tauri star candidates. For this purpose, we checked if the 56 sources previously classified as class II stars with photometric errors lower than 0.2 in WISE band 4 had blue colours in excess, i.e. if their $W1$, $W3$ and $W4$ magnitudes satisfy that $W1 - W3 \leq -1.7(W3 - W4) + 4.3$ (Koenig et al. 2012). Among the 56 class II sources found, we rejected nine based on this last criterion. On the other hand, protostellar objects with intermediate or high masses can be identified among class I sources by additionally requiring their band 3 (12 μm) magnitude to be less than 5 (Higuchi et al. 2013). All four class I WISE sources detected seem to be high-mass protostars, since all of them satisfy this criterion.

The cYSOs remaining in the final list are indicated in Fig. 11 and their fluxes and magnitudes are listed in Table 6.

4.2.2 Spatial distribution of cYSOs and possible formation scenarios

Fig. 11 shows that more than half of the cYSOS are on the PDR, with enhanced concentration at the locations of the molecular clumps C1, C2, C3 and C4 (see column 8 of Table 6), while the rest are projected towards the inner part of the H II region, where only faint molecular gas emission is detected at the velocity interval between 100 and 115 km s^{-1}, as delineated by the 0.3 K contour in Fig. 11.

On the other hand, we note that in the direction of the cYSOs located on C1, C2, C3 and C4, most of the CO profiles show one single radial component and when two or more components are detected, their intensities are considerably lower than the component within the velocity interval between +108 and +120 km s^{-1}. In contrast, in the direction to the rest of the cYSOs, several CO components are observed, as indicated in the last column of Table 6, where the radial velocities of the observed components are shown in decreasing order of their relative intensities. This suggests that several cYSOs are probably related to molecular gas at a different distance than G25.8700+0.1350, although the possibility that either they have already destroyed their entire natal cloud or that they are not protostellar objects cannot be discounted.

The observed spatial distribution of the cYSOs is a good indicator that the action of G25.8700+0.1350 on its environs is strong and could have triggered the formation of new stars. The estimated column densities (see Tables 2 and 3) are all above the threshold found by André et al. (2011), $N_{H2} \geq 7 \times 10^{21}$ cm^{-2}, indicating that star formation may well have taken place in all four clumps. Moreover, the mass–size relationship, which establishes that if $m(r) \geq 870\,M_\odot\,(r/pc)^{1.33}$ then the cloud can form high-mass stars (Kauffmann & Pillai 2010), is fulfilled by two of them, C1 and C2.

Radiation-driven implosion scenario. A close inspection of Fig. 11 suggests that radiation-driven implosion (RDI) could be at work in this region, since the molecular clump labelled C1 exhibits a cometary shape (see Section 3.4.2).

Radiative pressure from H II regions pushes away low-density gas more efficiently, and hence faster, than high-density gas, thus perturbing the structure and dynamics of molecular clouds. As a result, when an H II region finds dense molecular clumps along its expansion, bright rim clouds may form. When this happens, an IBL is developed around the clump and a photoionization front is driven into it. The subsequent evolution of the cloud is determined by the pressure balance between the internal molecular pressure and the external pressure of the IBL (Lefloch & Lazareff 1994).

Fig. 12 shows an enlarged view of the region of the clump C1. The cometary shape of the molecular cloud, shown through its Bolocam emission, is evident, as well as its bright IR border. Given their location with respect to the head of C1, the 2MASS sources 16, 17, 18 and 19 (asterisks in Fig. 12) are candidates for the O-type stars creating the IBL.

The cometary shape of the structure suggests that the RDI mechanism could be at work in this molecular cloud. Moreover, the presence of several cYSOs projected on to C1 (see Fig. 11) suggests that a star cluster has formed there and one of them has already given rise to the CHII region G025.7961+00.2403. To ascertain whether

Table 6. IRAS, MSX, WISE and *Spitzer* sources found to be cYSOs.

ID	Designation	(*l, b*) (°)	F_8 (Q_8) (Jy)	F_{12} (Q_{12}) (Jy)	F_{14} (Q_{14}) (Jy)	F_{21} (Q_{21}) (Jy)	Notes
			MSX sources				
1	G025.7961+00.2403	25.796, 0.2403	6.8488 (4)	8.4698 (4)	5.897 (4)	25.377 (4)	CHII, C1
2	G025.7597+00.1933	25.7597, 0.193	0.1439 (3)	1.304 (3)	1.0198 (2)	5.11 (4)	CHII
			WISE sources				
ID	Designation	(*l, b*) (°)	*W*1 (mag)	*W*2 (mag)	*W*3 (mag)	*W*4 (mag)	Notes
3	J183729.32-061225.2	25.820, 0.258	10.696 ± 0.079	9.186 ± 0.035	4.628 ± 0.021	2.730 ± 0.050	Class I, C1
4	J183726.58-061545.7	25.765, 0.243	10.435 ± 0.074	9.416 ± 0.061	4.498 ± 0.107	0.537 ± 0.020	Class I, C2
5	J183728.15-061559.8	25.765, 0.235	10.330 ± 0.071	9.329 ± 0.060	4.362 ± 0.094	1.123 ± 0.038	Class I, C2
6	J183730.52-061415.2	25.795, 0.240	7.550 ± 0.021	6.522 ± 0.019	1.219 ± 0.073	− 2.044 ± 0.016	Class I, C1
7	J183720.07-061447.9	25.767, 0.274	9.392 ± 0.026	8.739 ± 0.023	7.279 ± 0.039	4.088 ± 0.042	Class II, C2
8	J183732.00-061425.2	25.795, 0.233	10.189 ± 0.04	9.83 ± 0.046	5.602 ± 0.045	0.524 ± 0.022	Class II, C1
9	J183730.15-062034.0	25.701, 0.193	11.04 ± 0.058	10.692 ± 0.063	6.218 ± 0.065	1.223 ± 0.030	Class II, C3
10	J183726.91-061930.3	25.710, 0.213	11.615 ± 0.14	11.058 ± 0.146	6.721 ± 0.053	3.319 ± 0.064	Class II, C2
11	J183731.83-061404.8	25.800, 0.236	9.077 ± 0.029	8.52 ± 0.029	4.707 ± 0.028	0.658 ± 0.055	Class II, C1
12	J183721.37-061325.2	25.790, 0.280	9.519 ± 0.028	8.92 ± 0.028	7.497 ± 0.075	3.862 ± 0.029	Class II, C1
13	J183731.37-061402.1	25.800, 0.238	8.16 ± 0.024	7.600 ± 0.024	3.877 ± 0.086	− 0.978 ± 0.030	Class II, C1
14	J183734.68-062018.6	25.713, 0.178	9.999 ± 0.035	9.579 ± 0.046	4.707 ± 0.026	2.802 ± 0.036	Class II, C3
15	J183746.69-062218.8	25.706, 0.119	9.345 ± 0.029	9.029 ± 0.027	5.453 ± 0.025	3.673 ± 0.061	Class II, C4
16	J183724.91-061434.8	25.779, 0.258	10.15 ± 0.0554	9.744 ± 0.069	5.28 ± 0.028	1.853 ± 0.023	Class II, C1
17	J183725.21-061526.0	25.767, 0.250	9.638 ± 0.034	9.225 ± 0.04	5.229 ± 0.05	1.53 ± 0.027	Class II, C2
18	J183732.37-061324.2	25.811, 0.240	10.864 ± 0.057	10.4 ± 0.073	6.883 ± 0.121	1.286 ± 0.069	Class II, C1
19	J183746.38-062153.6	25.712, 0.123	8.308 ± 0.023	7.854 ± 0.023	6.091 ± 0.034	4.188 ± 0.072	Class II, C4
20	J183728.71-061606.4	25.764, 0.232	10.173 ± 0.078	9.589 ± 0.053	4.77 ± 0.059	0.898 ± 0.028	Class II, C2
21	J183720.95-061508.7	25.764, 0.268	9.939 ± 0.031	9.548 ± 0.032	5.264 ± 0.022	1.967 ± 0.023	Class II, C2
22	J183732.07-062116.5	25.694, 0.181	10.792 ± 0.05	9.996 ± 0.045	7.387 ± 0.105	3.731 ± 0.054	Class II, C3
23	J183727.95-061159.4	25.824, 0.267	9.5 ± 0.05	8.816 ± 0.032	4.605 ± 0.027	4.878 ± 0.199	Class II, C1
24	J183724.91-061449.6	25.776, 0.256	10.77 ± 0.066	10.047 ± 0.067	5.189 ± 0.027	2.492 ± 0.058	Class II, C1
25	J183731.33-061828.3	25.734, 0.205	10.262 ± 0.037	9.367 ± 0.033	4.484 ± 0.035	1.442 ± 0.043	Class II, C2
26	J183746.75-062236.7	25.702, 0.116	10.389 ± 0.038	9.933 ± 0.035	6.596 ± 0.046	4.499 ± 0.108	Class II, C4
27	J183714.88-061522.2	25.749, 0.289	5.587 ± 0.123	4.936 ± 0.064	3.359 ± 0.017	2.074 ± 0.018	Class II, C2
28	J183731.91-062020.5	25.707, 0.188	10.895 ± 0.065	9.914 ± 0.046	6.644 ± 0.043	2.424 ± 0.053	Class II, C3
29	J183731.09-060932.4	25.866, 0.274	10.868 ± 0.049	10.467 ± 0.046	7.521 ± 0.065	6.633 ± null	Class II, C1
30	J183727.40-061714.7	25.745, 0.229	10.352 ± 0.067	9.991 ± 0.0414	5.598 ± 0.041	1.654 ± 0.030	Class II, C2
31	J183728.07-061716.6	25.746, 0.226	10.597 ± 0.062	10.002 ± 0.044	5.443 ± 0.058	1.17 ± 0.023	Class II, C2
32	J183726.23-061207.7	25.818, 0.272	10.883 ± 0.109	10.26 ± 0.076	5.504 ± 0.033	2.608 ± 0.046	Class II, C1
33	J183724.66-061443.1	25.777, 0.258	11.037 ± 0.076	10.056 ± 0.071	5.243 ± 0.032	1.973 ± 0.035	Class II, C1
34*	J183732.95-062018.7	25.710, 0.185	8.882 ± 0.028	8.419 ± 0.025	4.519 ± 0.021	3.456 ± 0.062	Class II, C3
35	J183725.03-061515.4	25.770, 0.252	10.402 ± 0.037	9.728 ± 0.042	5.351 ± 0.053	2.036 ± 0.037	Class II, C1
36	J183730.25-062047.2	25.698, 0.191	10.752 ± 0.057	10.298 ± 0.049	7.171 ± 0.135	1.568 ± 0.026	Class II, C3
37	J183725.12-061500.3	25.774, 0.254	10.32 ± 0.049	9.947 ± 0.065	5.316 ± 0.029	2.108 ± 0.040	Class II, C1
38	J183721.48-061309.7	25.794, 0.282	9.442 ± 0.031	8.765 ± 0.027	6.646 ± 0.032	4.136 ± 0.028	Class II, C1
39	J183723.96-061446.6	25.775, 0.260	11.475 ± 0.109	10.898 ± 0.141	7.26 ± 0.148	2.967 ± 0.065	Class II, C1
40	J183805.93-060741.8	25.959, 0.160	10.944 ± 0.043	10.569 ± 0.051	7.426 ± 0.116	4.443 ± 0.136	Class II, 100 km s^{-1}
41	J183810.23-061515.0	25.856, 0.087	9.714 ± 0.029	9.305 ± 0.031	7.335 ± 0.086	4.762 ± 0.117	Class II, 30 km s^{-1}
42	J183817.35-061815.5	25.825, 0.0374	9.912 ± 0.028	9.525 ± 0.031	7.433 ± 0.117	4.574 ± 0.060	Class II, 100 km s^{-1}
43	J183747.97-061326.5	25.840, 0.182	9.771 ± 0.03	9.276 ± 0.026	7.603 ± 0.134	5.187 ± 0.136	Class II, 100 km s^{-1}
44	J183812.35-060918.5	25.948, 0.124	8.132 ± 0.035	7.391 ± 0.021	6.202 ± 0.029	4.151 ± 0.039	Class II, 100 km s^{-1}
45	J183751.67-062025.4	25.744, 0.115	8.204 ± 0.026	7.78 ± 0.023	6.24 ± 0.023	1.543 ± 0.060	Class II, 30 and 100 km s^{-1}
46	J183745.91-060510.9	25.959, 0.253	8.994 ± 0.027	8.518 ± 0.023	7.088 ± 0.066	4.981 ± 0.274	Class II, 100 km s^{-1}
47	J183812.05-061227.1	25.901, 0.101	10.487 ± 0.04	9.721 ± 0.036	8.163 ± 0.096	6.295 ± 0.207	Class II, 100 km s^{-1}
48	J183810.70-060807.3	25.962, 0.139	10.579 ± 0.043	10.255 ± 0.038	7.502 ± 0.09	5.793 ± 0.116	Class II, 100 km s^{-1}
49	J183815.45-061755.5	25.826, 0.0470	9.639 ± 0.079	8.95 ± 0.07	6.346 ± 0.118	4.01 ± 0.081	Class II, 100 km s^{-1}
50	J183743.67-060833.7	25.905, 0.235	10.657 ± 0.037	9.818 ± 0.037	7.753 ± 0.115	2.578 ± 0.027	Class II, 70 and 100 km s^{-1}
51	J183759.17-062006.6	25.763, 0.090	6.336 ± 0.05	5.796 ± 0.025	3.14 ± 0.016	1.373 ± 0.024	Class II, 30 and 100 km s^{-1}
52	J183757.75-061054.6	25.897, 0.166	6.126 ± 0.108	5.486 ± 0.06	3.962 ± 0.017	2.626 ± 0.028	Class II, 65 and 100 km s^{-1}
53	J183752.61-061021.2	25.895, 0.189	10.814 ± 0.062	10.115 ± 0.045	8.106 ± 0.102	6.485 ± 0.144	Class II, 65 and 100 km s^{-1}
54	G025.7443+00.1845	25.744, 0.184	12.156 ± 0.08	11.027 ± 0.06	10.16 ± 0.072	9.955 ± 0.146	Class I
55	G025.7967+00.2764	25.796, 0.276	12.3 ± 0.058	11.463 ± 0.098	10.565 ± 0.095	9.796 ± 0.113	Class I, C1
56	G025.7943+00.2827	25.794, 0.282	9.937 ± 0.05	9.146 ± 0.043	8.395 ± 0.039	7.856 ± 0.0454	Class I, C1
57	G025.7619+00.1029	25.762, 0.103	12.421 ± 0.058	10.408 ± 0.11	8.896 ± 0.039	8.025 ± 0.046	Class I, 30, 60, and 100 km s^{-1}
58	G025.8895+00.0917	25.889, 0.091	13.512 ± 0.088	12.063 ± 0.088	11.088 ± 0.108	10.379 ± 0.0854	Class I, 100 and 30 km s^{-1}
59	G025.7978+00.0736	25.797, 0.073	12.572 ± 0.08	11.321 ± 0.087	10.416 ± 0.074	9.886 ± 0.064	Class I, 30 and 60 km s^{-1}

Table 6 – *continued*

ID	Designation	(*l*, *b*) (°)	Spitzer sources 4.5 μm (mag)	5.8 μm (mag)	8.0 μm (mag)	24 μm (mag)	Notes
60	G025.8564+00.0781	25.856, 0.078	12.506 ± 0.096	11.643 ± 0.061	10.878 ± 0.094	10.567 ± 0.085	Class I, 100, 120, 60, and 30 km s^{-1}
61	G025.8320+00.0735	25.832, 0.073	13.609 ± 0.128	11.896 ± 0.146	10.567 ± 0.07	9.941 ± 0.057	Class I, 30, 40, 100 km s^{-1}
62	G025.8991+00.1062	25.899, 0.106	12.735 ± 0.079	11.552 ± 0.08	10.507 ± 0.083	9.378 ± 0.042	Class I, 100, 30, 60 km s^{-1}
63	G025.7545+00.2578	25.754, 0.257	11.246 ± 0.077	10.262 ± 0.059	9.564 ± 0.055	9.021 ± 0.06	Class II, C2
64	G025.7212+00.2476	25.721, 0.247	8.775 ± 0.043	8.335 ± 0.049	7.761 ± 0.033	7.4 ± 0.032	Class II, C2
65	G025.8269+00.1224	25.827, 0.122	8.544 ± 0.05	8.289 ± 0.041	7.76 ± 0.034	7.405 ± 0.029	Class II, 90, 100, 30 km s^{-1}
66	G025.7900+00.1191	25.790, 0.119	12.4 ± 0.078	11.738 ± 0.074	11.351 ± 0.1	10.333 ± 0.079	Class II, 30 km s^{-1}
67	G025.7754+00.1288	25.775, 0.128	8.893 ± 0.041	8.602 ± 0.046	8.338 ± 0.039	7.925 ± 0.033	Class II, 30 km s^{-1}
68	G025.9598+00.1602	25.959, 0.160	10.815 ± 0.0414	10.412 ± 0.079	10.134 ± 0.059	9.238 ± 0.059	Class II, 100 km s^{-1}
69	G025.9303+00.1309	25.930, 0.131	10.868 ± 0.051	10.298 ± 0.0584	9.749 ± 0.059	8.926 ± 0.043	Class II, 100, 60 km s^{-1}
70	G025.7820+00.0632	25.782, 0.063	9.801 ± 0.06	9.15 ± 0.051	8.59 ± 0.039	7.702 ± 0.029	Class II, 30, 110 km s^{-1}
71	G025.8833+00.2496	25.883, 0.249	10.020 ± 0.045	9.351 ± 0.053	8.719 ± 0.036	7.873 ± 0.048	Class II, 100, 70 km s^{-1}
72	G025.8383+00.2416	25.838, 0.241	12.622 ± 0.073	12.022 ± 0.097	11.685 ± 0.151	10.532 ± 0.103	Class II, 100, 70 km s^{-1}
73	G025.8281+00.1596	25.828, 0.159	12.009 ± 0.0954	11.106 ± 0.106	10.454 ± 0.079	9.781 ± 0.061	Class II, 100, 30, 60 km s^{-1}
74	G025.8786+00.1662	25.878, 0.166	11.467 ± 0.069	11.035 ± 0.129	10.685 ± 0.067	10.099 ± 0.054	Class II, 60, 70, 100 km s^{-1}
75	G025.8865+00.1622	25.886, 0.162	11.923 ± 0.056	11.406 ± 0.071	10.775 ± 0.097	10.2 ± 0.066	Class II, 60, 70, 100 km s^{-1}
76	G025.8133+00.1824	25.813, 0.182	11.854 ± 0.111	11.269 ± 0.079	10.983 ± 0.073	10.229 ± 0.08	Class II, 100, 60 km s^{-1}
77	G025.8548+00.1909	25.855, 0.191	12.254 ± 0.104	11.605 ± 0.116	11.117 ± 0.088	9.737 ± 0.081	Class II, 100, 60 km s^{-1}
78	G025.8952+00.1889	25.895, 0.189	10.405 ± 0.04	9.823 ± 0.057	9.148 ± 0.044	8.433 ± 0.034	Class II, 100, 60, 70 km s^{-1}

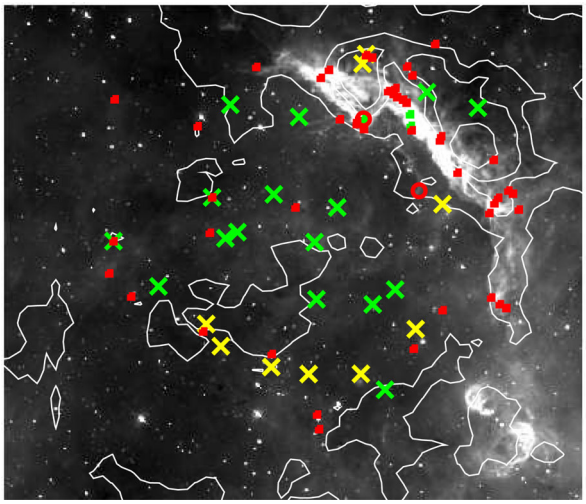

Figure 11. *Spitzer* 8 μm emission distribution showing the PDR. Contour levels at 0.3, 0.8, 1.0 and 1.3 K delineate the average ^{13}CO emission between 100 and 115 km s^{-1}. The red circles indicate the location of the MSX sources. Green and red squares correspond to WISE class I and II cYSOs, respectively. Yellow and green crosses indicate *Spitzer* class I and II sources, respectively.

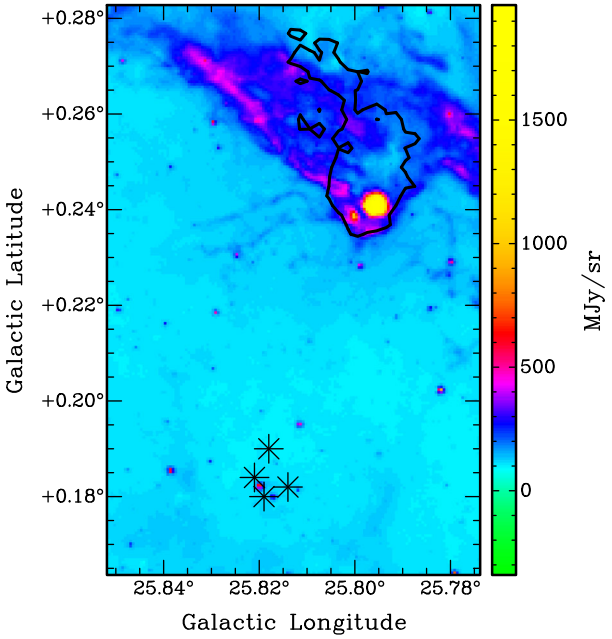

Figure 12. *Spitzer* image at 8 μm of the region of the C1 source. The contour indicates the 1.1 mm emission at 0.3 Jy beam^{-1}. The four asterisks show the location of the 2MASS sources that are candidate O-type stars (16, 17, 18 and 19 in Table 5 and Fig. 8).

this is the case, both the inner pressure and outer pressure acting on the clump have to be estimated and compared.

The pressure in the IBL can be evaluated from the electron density in the boundary layer, n_e, as $P_i = 2n_e m_H c_i^2$, where $m_H = 1.67 \times 10^{-24}$ g is the mass of the hydrogen atom and c_i is the speed of sound in the ionized gas ($c_i \sim 14$ km s^{-1}). A rough estimate of n_e can be obtained using the spherical model of Mezger & Henderson (1967) with an appropriate filling factor f to account for the fraction of the assumed sphere that actually contains ionized gas:

$$n_e = 533.5\, T_4^{0.175}\, \nu_{GHz}^{0.05}\, S_\nu^{0.5}\, (f^{1/3}\theta)^{-1.5}\, D_{kpc}^{-0.5}\ \mathrm{cm}^{-3},$$

where S_ν is the measured flux density in janskys, θ the angular width in minutes of arc, T_4 the electron temperature in units of 10^4 K, D_{kpc} the distance in kiloparsecs and ν_{GHz} the frequency in gigahertz.

Based on the MAGPIS 1.42 GHz image, we obtained a flux density $S_{1.42} = 120 \pm 30$ mJy for the emission observed in the border of C1. Then, assuming a distance of 6.5 ±1.0 kpc, a temperature of 6120 ± 100 K, the C1 angular width, $\theta = 4 \pm 1$ arcmin and $f = 0.03$, we obtain $n_e = 70 \pm 30$ cm^{-3} and $P_i/k = (3.3 \pm 1.4) \times 10^6$ cm^{-3} K.

As mentioned above, this pressure should be compared with the pressure of the molecular cloud, which can be estimated, assuming

that the thermal component can be neglected, from the turbulent velocity dispersion σ^2 and the molecular density ρ_m as $P_{\rm m} = \sigma^2 \rho_m$, where σ^2 may be written as $\sigma^2 = \Delta v^2/(8 \ln 2)$, Δv being the observed velocity line width of the molecular cloud gas. Adopting for C1 the ambient density given in Table 2, $n_{\rm H2} = 2.1 \times 10^3$ cm^{-3}, and $\Delta v = 4.8 \pm 0.7$ km s^{-1}, we infer a molecular pressure $P_{\rm m}/k = (2.8 \pm 1.2) \times 10^{-6}$ cm^{-3} K, assuming a 30 per cent error in the molecular density.

Since the pressures $P_{\rm i}$ and $P_{\rm m}$ obtained for C1 are similar, the ionized and molecular gas seem to be in pressure balance and the propagation of a photoionization-induced shock into the molecular gas may have occurred.

5 SUMMARY

We have carried out a multi-wavelength study of the ionized region G25.8700+0.1350 to characterize the physical properties of the related gas and dust and to investigate its possible origin and role in forming new stars. Based on data obtained from several surveys, we arrived at the following results:

(i) Since G25.8700+0.1350 is in the first Galactic quadrant and close to the tangent point, its distance was not clear. Based on a comparison of H I absorption profiles, in this work we solved the distance ambiguity and determined a distance of 6.5 ±1.0 kpc from the Sun, which corresponds to the near distance.

(ii) The region is very bright in the 1420 MHz radio continuum. It contains about 2500 $M_\odot$ of ionized gas, and at least 5×10^{49} photons s^{-1} are needed to keep it ionized. This implies that several O-type stars, which have not been detected yet, should be located in this part of the Galaxy.

(iii) The ^{13}CO (1-0) and 1.1 mm data reveal the presence of four clumps bordering the H II region. These were detected in the velocity range approximately from 106 to 116 km s^{-1}, compatible with the velocity of the RRLs detected in the region. Based on their estimated physical properties, we conclude that all these clumps are capable of forming new stars and, in particular, clumps C1 and C2 may contain high-mass protostars.

(iv) At IR wavelengths, we identified an unmistakable PDR in the interface between the ionized and molecular gas. The *Herschel* data show that the region is also detected in the far-IR. We found that the dust temperature goes from about 21 K in the cold clumps up to 31 K in the region more directly exposed to stellar radiation.

(v) Since G25.8700+0.1350 is located in the inner galaxy, where the visual extinction is high, the candidate ionizing stars had to be searched for in the IR. There is one WR star, HDM 40, and one RSG, 18375756-0620155, that may be related to the region. On the other hand, based on colour criteria, we identified 37 2MASS sources that could be O-type ionizing stars.

(vi) Applying different colour criteria, 78 cYSOs have been identified in the region, of which 44 are projected on to the molecular gas related to G25.8700+0.1350. Based on the observed distribution of both the IR and molecular emission, we propose that the RDI mechanism has taken place on to C1 and triggered the formation of the high-mass star responsible for the striking CHII region G025.7961+00.2403.

ACKNOWLEDGEMENTS

This work is dedicated to the memory of our dear colleague Gisela Romero. We are grateful to the referee for their very constructive input. VGPS is supported by grants from the Natural Sciences and Engineering Research Council of Canada and from the US National Science Foundation. The National Radio Astronomy Observatory is a facility of the National Science Foundation operated under cooperative agreement by Associated Universities, Inc. This research made use of the NASA/IPAC Infrared Science Archive, which is operated by the Jet Propulsion Laboratory, California Institute of Technology, under contract with the National Aeronautics and Space Administration (NASA). *Herschel* is an ESA space observatory with science instruments provided by European-led principal investigator consortia and with important participation from NASA. This work is partially based on observations made with the *Spitzer Space Telescope*, which is operated by the Jet Propulsion Laboratory, California Institute of Technology, under a contract with NASA. This publication makes use of molecular line data from the Boston University-FCRAO Galactic Ring Survey, which is a joint project of Boston University and Five College Radio Astronomy Observatory, funded by the National Science Foundation under grants AST-9800334, AST-0098562 and AST-0100793. This project was partially financed by the Consejo Nacional de Investigaciones Cientificas y Tecnicas (CONICET) of Argentina under projects PIP 01299, PIP 0226, PIP 00356 and PIP 00107, and Universidad Nacional de La Plata under 2012-2014 PPID/G002 and 11/G120.

REFERENCES

Aguirre J. E. et al., 2011, ApJS, 192, 4
Anderson L. D., Bania T. M., 2009, ApJ, 690, 706
Anderson L. D., Bania T. M., Jackson J. M., Clemens D. P., Heyer M., Simon R., Shah R. Y., Rathborne J. M., 2009, ApJS, 181, 255
Anderson L. D., Bania T. M., Balser D. S., Cunningham V., Wenger T. V., Johnstone B. M., Armentrout W. P., 2014, ApJS, 212, 1
André P., Men'shchikov A., Könyves V., Arzoumanian D., 2011, in Alves J., Elmegreen B. G., Girart J. M., Trimble V., eds, Proc. IAU Symp. 270, Computational Star Formation. Univ. Press, Cambridge, p. 255
Benjamin R. A. et al., 2003, PASP, 115, 953
Cazzolato F., Pineault S., 2005, AJ, 129, 2731
Chaisson E. J., 1976, in Avrett E. H., ed., Frontiers of Astrophysics. Harvard Univ. Press, Cambridge, p. 259
Chen B., Figueras F., Torra J., Jordi C., Luri X., Galadí-Enríquez D., 1999, A&A, 352, 459
Comerón F. et al., 2002, A&A, 389, 874
Cutri R. M. et al., 2003, 2MASS All Sky Catalog of point sources. The IRSA 2MASS All-Sky Point Source Catalog, NASA/IPAC Infrared Science Archive. Available at: http://irsa.ipac.caltech.edu/applications/Gator/
Dame T. M., Hartmann D., Thaddeus P., 2001, ApJ, 547, 792
Davies B., Figer D. F., Kudritzki R.-P., MacKenty J., Najarro F., Herrero A., 2007, ApJ, 671, 781
Davies B., Figer D. F., Law C. J., Kudritzki R.-P., Najarro F., Herrero A., MacKenty J. W., 2008, ApJ, 676, 1016
Dempsey J. T., Thomas H. S., Currie M. J., 2013, ApJS, 209, 8
Dickman R. L., 1978, ApJS, 37, 407
Dorda R., Negueruela I., González-Fernández C., Marco A., 2016, in Skillen I., Barcells M., Trager S., eds, ASP Conf. Ser. Vol. 507, Multi-Object Spectroscopy in the Next Decade: Big Questions, Large Surveys, and Wide Fields. Astron. Soc. Pac., San Francisco, p. 165
Draine B. T. et al., 2007, ApJ, 663, 866
Drilling J. S., Landolt A. U., 2000, in Cox A. N., ed., Normal Stars. AIP Press; Springer, New York, NY, p. 381
Egan M. P., Price S. D., Kraemer K. E., 2003, BAAS, 35, 1301
Ekström S. et al., 2012, A&A, 537, A146
Ekström S., Georgy C., Meynet G., Groh J., Granada A., 2013, in Kervella P., Le Bertre T., Perrin G., eds, EAS Publ. Ser., 60, 31
Elmegreen B. G., Lada C. J., 1977, ApJ, 214, 725

Fich M., Blitz L., Stark A. A., 1989, ApJ, 342, 272
Figer D. F., MacKenty J. W., Robberto M., Smith K., Najarro F., Kudritzki R. P., Herrero A., 2006, ApJ, 643, 1166
Glenn J. et al., 2003, in Phillips T. G., Zmuidzinas J., eds, Proc. SPIE 4855, Millimeter and Submillimeter Detectors for Astronomy. SPIE, Bellingham, p. 30
Griffin M. J. et al., 2010, A&A, 518, L3
Gutermuth R. A., Megeath S. T., Myers P. C., Allen L. E., Pipher J. L., Fazio G. G., 2009, ApJS, 184, 18
Helfand D. J., Becker R. H., White R. L., Fallon A., Tuttle S., 2006, AJ, 131, 2525
Higuchi A. E., Kurono Y., Naoi T., Saito M., Mauersberger R., Kawabe R., 2013, ApJ, 765, 101
Hildebrand R. H., 1983, QJRAS, 24, 267
Hollenbach D. J., Tielens A. G. G. M., 1997, ARA&A, 35, 179
Jackson J. M. et al., 2006, ApJS, 163, 145
Kauffmann J., Pillai T., 2010, ApJ, 723, L7
Koenig X. P., Leisawitz D. T., Benford D. J., Rebull L. M., Padgett D. L., Assef R. J., 2012, ApJ, 744, 130
Kos J. et al., 2014, Science, 345, 791
Lefloch B., Lazareff B., 1994, A&A, 289, 559
Levesque E. M., Massey P., Olsen K. A. G., Plez B., Josselin E., Maeder A., Meynet G., 2005, ApJ, 628, 973
Lockman F. J., Pisano D. J., Howard G. J., 1996, ApJ, 472, 173
Lumsden S. L., Hoare M. G., Oudmaijer R. D., Richards D., 2002, MNRAS, 336, 621
Martins F., Plez B., 2006, A&A, 457, 637
Martins F., Schaerer D., Hillier D. J., 2005, A&A, 436, 1049
Mauerhan J. C., Van Dyk S. D., Morris P. W., 2011, AJ, 142, 40
Mezger P. G., Henderson A. P., 1967, ApJ, 147, 471
Molinari S. et al., 2010, PASP, 122, 314
Negueruela I., Marco A., González-Fernández C., Jiménez-Esteban F., Clark J. S., Garcia M., Solano E., 2012, A&A, 547, A15
Oka T., Onodera Y., Nagai M., Tanaka K., Matsumura S., Kamegai K., 2012, ApJS, 201, 14
Ossenkopf V., Henning T., 1994, A&A, 291, 943
Poglitsch A. et al., 2010, A&A, 518, L2
Quireza C., Rood R. T., Balser D. S., Bania T. M., 2006a, ApJS, 165, 338
Quireza C., Rood R. T., Bania T. M., Balser D. S., Maciel W. J., 2006b, ApJ, 653, 1226
Reynoso E. M., Cichowolski S., Walsh A. J., 2017, MNRAS, 464, 3029
Rieke G. H., Lebofsky M. J., 1985, ApJ, 288, 618
Rieke G. H. et al., 2004, ApJS, 154, 25
Schlafly E. F., Finkbeiner D. P., 2011, ApJ, 737, 103
Schnee S. L., Ridge N. A., Goodman A. A., Li J. G., 2005, ApJ, 634, 442
Sewilo M., Watson C., Araya E., Churchwell E., Hofner P., Kurtz S., 2004, ApJS, 154, 553
Shirley Y. L. et al., 2013, ApJS, 209, 2
Stil J. M. et al., 2006, AJ, 132, 1158
Strong A. W., Mattox J. R., 1996, A&A, 308, L21
Tokunaga A. T., 2000, in Cox A. N., ed., Infrared Astronomy. AIP Press; Springer, New York, NY, p. 143
Weaver R., McCray R., Castor J., Shapiro P., Moore R., 1977, ApJ, 218, 377
Werner M. W. et al., 2004, ApJS, 154, 1
Whittet D. C. B., ed., 2003, Dust in the Galactic Environment, 2nd ed. IoP Publishing, Bristol
Wright E. L. et al., 2010, AJ, 140, 1868
Zinnecker H., Yorke H. W., 2007, ARA&A, 45, 481

This paper has been typeset from a TEX/LATEX file prepared by the author.